MEASUREMENT OF HELIUM FLUX AND VARIABILITY IN LOW EARTH ORBIT WITH THE ALPHA MAGNETIC SPECTROMETER

A THESIS SUBMITTED TO
THE GRADUATE SCHOOL OF NATURAL AND APPLIED SCIENCES
OF
MIDDLE EAST TECHNICAL UNIVERSITY

BY

GÜLCE KARAGÖZ

IN PARTIAL FULFILLMENT OF THE REQUIREMENTS
FOR
THE DEGREE OF MASTER OF SCIENCE
IN
PHYSICS

FEBRUARY 2022

Approval of the thesis:

MEASUREMENT OF HELIUM FLUX AND VARIABILITY IN LOW EARTH ORBIT WITH THE ALPHA MAGNETIC SPECTROMETER

submitted by **GÜLCE KARAGÖZ** in partial fulfillment of the requirements for the degree of **Master of Science in Physics Department, Middle East Technical University** by,

Prof. Dr. Halil Kalıpçılar
Dean, Graduate School of **Natural and Applied Sciences** _____

Prof. Dr. Seçkin Kürkçüoğlu
Head of Department, **Physics** _____

Prof. Dr. Melahat Bilge Demirköz
Supervisor, **Physics, METU** _____

Examining Committee Members:

Prof. Dr. Altuğ Özpineci
Physics, METU _____

Prof. Dr. Melahat Bilge Demirköz
Physics, METU _____

Prof. Dr. İsmail Turan
Physics, METU _____

Prof. Dr. Ali Murat Güler
Physics, METU _____

Prof. Dr. Yamaç Pehlivan
Physics, MSGSÜ _____

Date: 10.02.2022

I hereby declare that all information in this document has been obtained and presented in accordance with academic rules and ethical conduct. I also declare that, as required by these rules and conduct, I have fully cited and referenced all material and results that are not original to this work.

Name, Surname: Gülce Karagöz

Signature :

ABSTRACT

MEASUREMENT OF HELIUM FLUX AND VARIABILITY IN LOW EARTH ORBIT WITH THE ALPHA MAGNETIC SPECTROMETER

Karagöz, Gülce
M.S., Department of Physics
Supervisor: Prof. Dr. Melahat Bilge Demirköz

February 2022, 82 pages

The Alpha Magnetic Spectrometer (AMS-02) is an unrivalled particle physics detector with a large magnet whose aim is to search for anti-matter and dark matter by performing measurements on cosmic ray composition and flux. AMS-02 has been operating on the International Space Station (ISS) since its launch on the 16th May 2011, and is planned to operate along the lifetime of the ISS. AMS-02 has a unique design with a large acceptance and sensitive detection of cosmic rays, allowing one to better understand the acceleration and origin of cosmic rays. Helium nuclei are the second most abundant nuclei in the cosmic ray composition and since Helium has the smallest cross-section among the cosmic ray nuclei, it interacts the least with the interstellar medium, which means that the helium nuclei can travel from the furthest points of the galaxy. In this work, helium nuclei spectrum is studied in two parts. The first one is the time-independent helium flux, in which the flux is investigated in a large energy range up to 1.2TV. The second is the time-dependent helium flux, where the flux is investigated in a smaller energy scale in which our Sun dominates with its contribution.

Keywords: AMS-02, helium flux, cosmic ray, solar modulation

ÖZ

ALFA MANYETİK SPEKTROMETRESİ İLE DÜŞÜK DÜNYA YÖRÜNGESİNDE HELYUM AKISININ ÖLÇÜMÜ VE DEĞİŞİMİ

Karagöz, Gülce
Yüksek Lisans, Fizik Bölümü
Tez Yöneticisi: Prof. Dr. Melahat Bilge Demirköz

Şubat 2022 , 82 sayfa

Alfa Manyetik Spektrometresi (AMS-02) amacı anti madde ve karanlık maddeyi kozmik ışın spetrumunun içeriğini ve akısını ölçerek araştırmak olan, büyük bir mıknatısa sahip emsalsiz bir parçacık fiziği dedektörüdür. AMS-02, Uluslararası Uzay İstasyonu (UUİ)'na yerleştirildiği 16 Mayıs 2011'den beri operasyoneldir ve UUİ'nin görev süresince çalışmaya devam etmesi planlanmaktadır. AMS-02'nin, kozmik ışınların ivmelenmesinin ve yayılımının anlaşılmasını sağlayan, yüksek bir kabul oranına ve hassas bir ölçüm imkanına olanak sağlayan eşsiz bir dizaynı vardır. Helyum, kozmik ışın spektrumundaki en baskın ikinci çekirdektir ve bütün kozmik ışınlar içindeki en düşük etkileşim kesitine sahiptir, bu nedenle yıldızlararası ortam ile en az etkileşir, bu da helyumun evrenin en uzak noktalarından yayılımına olanak sağlamaktadır. Bu çalışmada helyum çekirdeği spektrumu iki bölümde incelenmiştir. İlk kısım helyumun zamandan bağımsız akısını içermektedir, burada helyum akısının 1.2TV'ye kadar analizi yapılmıştır. İkinci kısım ise helyumun zamana bağlı akısını içermektedir ve daha düşük bir enerji aralığında çalışılmıştır ve bu aralıkla akı, kendi Güneş'imiz tarafından baskılanmaktadır.

Anahtar Kelimeler: AMS-02, helyum akısı, kozmik ışınlar, Güneş modülasyonu

To never giving up.

ACKNOWLEDGMENTS

Working with CERN AMS-02 group is an unique opportunity and I want express my deep thanks to my advisor Prof.Melahat Bilge Demirköz. She was always there as an advisor when I was struggling with life and physics (I do not know which one is harder). From the moment she let me join her group she was so supportive and encouraging. She believed in me even in the times I feel hopeless and thinking about giving up. Words are not enough to express my greatefulness to her.

I would like to thank Prof. Samuel C.C. Ting, for letting me join this valuable research which explores the biggest adventure of human history. I want to thank Cristina Consolandi for her discussions on my work and her kindness. I want to express my gratitues to Senquan Lu, who always helped me while carrying out this analysis and guided me with patience everytime I asked him questions.

I would like to thank all of my colleagues and the friends from METU-IVMER especially Cenk Tüysüz and Raheem Hashmani who shared all the coding knowledge from the first bracket to the last. Also for Berk Türk, who joined the group lately but helped as if he was always there. Lastly I want to thank Erinç Kılıç, Brunilda Muçogllava and Arda Kayaalp for their amusing "officeship".

Last but not least, I want to thank my friends Cansu Ellialtıoğlu, Simge Yalçın, Şeyma Koçak and Elif Nur Bayer for their support and encourage on this long journey. Having a life with physics would almost be impossible with your absence.

Finally, I want to thank my mother Asiye Karagöz and my father Metin Karagöz for every opportunity they have provided me and their endless trust in me. I owe to them who I am today. Also my cat Zeytin, who always there to pull off the cables of my computer and scatter the notes I had taken.

I would like to acknowledge that this work is supported by Turkish Atomic Energy Authority (TAEK) (Grant No:2020TAEK(CERN)A5.H1.F5-26).

TABLE OF CONTENTS

LIST OF TABLES

LIST OF FIGURES

FIGURES

LIST OF ABBREVIATIONS

AMS-02	Alpha Magnetic Spectrometer-02
CR	Cosmic Ray
ISS	International Space Station
LEO	Low Earth Orbit
ToF	Time of Flight
TRD	Transition Radiation Detector
ST	Silicon Tracker
ECAL	Electromagnetic Calorimeter
RICH	Ring Image Cherenkov Detector
MC	Monte Carlo
FGST	Fermi Gamma-Ray Space Telescope
PAMELA	Payload for Antimatter Matter Exploration and Light nuclei Astrophysics
GZK	Greisen-Zatsepin-Kuzmin (Cutoff)
SEP	Solar Energetic Particle
CME	Coronal Mass Ejection
SNR	Supernova Remnant
GCR	Galactic Cosmic Ray
UHECR	Ultra High Energetic Cosmic Ray
CMBR	Cosmic Microwave Background Radiation
ISM	Interstellar Medium
SAA	South Atlantic Anomaly
TRDS	Tracking and Data Relay Satellite
POCC	Payload Operations and Control Center

PMT	Photo Multiplier Tube
LT	Low Threshold
MIP	Minimum Ionization Particle
HT	High Threshold
SHT	Super High Threshold
TR	Transition Radiation
ACC	Anti Coincidence Counter
GV	Gigavolt
TV	Teravolt
FS	Full Span

CHAPTER 1

INTRODUCTION

The environment in space is very different than the surface of the Earth. Astrophysical sources such as supernova remnants, neutrino stars, pulsars, and even our Sun radiate and accelerate charged particles in the plasma surrounding them. Thanks to the Earth's geomagnetic environment and its atmosphere, Earth is protected from a significant fraction of these accelerated particles. Low energetic charged particles get trapped in the magnetic field of the Earth in Van Allen Belts. In contrast, energetic charged particles can escape the magnetic field of the Earth, but some of them enter the atmosphere, and a few can reach the surface of the Earth.

Alpha Magnetic Spectrometer-02 (AMS-02) is a particle physics detector that has been on International Space Station (ISS) operating in Low Earth Orbit(LEO) since 16 May 2011. It is a high precision magnetic spectrometer that can measure the particles coming from astrophysical sources up to very high energies that were not reached before[3]. AMS-02 is a multi-purpose detector that consists of different sub-detectors, which are Time of Flight (ToF), Silicon Tracker, Electromagnetic Calorimeter (ECAL), Ring Image Cherenkov Detector (RICH), and each of them has different functionality. Together with these sub-detectors, AMS-02 can identify the charge, mass and momentum of the particle.

Helium is the second most abundant nuclei in the cosmic ray composition. Due to its small cross-section, it does not interact with the interstellar medium as much as heavier nuclei, making propagation from the furthest edge of the galaxy possible. In this work, the average flux of Helium from 2011 to 2020 is analyzed. Sub-detector efficiencies and cuts applied to select the relevant nuclei, the stages for computing the average flux, such as computing exposure time, efficiencies of sub-detectors as

well as acceptance calculations are discussed. Finally, a time-dependent analysis is performed, and periodicities concerning Bartels rotation are discussed [4].

In the second chapter, cosmic ray phenomenology is presented. The history and energy spectrum of cosmic rays and their composition, interactions of charged particles with the interstellar medium are briefly discussed. Detection methods of cosmic rays are exemplified by basic experiments and the physics ideas behind them. In the third chapter, AMS-02, its purpose, functionalities of sub-detectors, and their layout are presented. The data acquisition system and the Monte Carlo simulations are also discussed. In the fourth chapter, sub-detector efficiencies are presented for each applied cut and the functionality of each cut is explained. The fifth chapter is dedicated to the time-dependent Helium flux, its calculation, and the results are presented and discussed. In the final chapter, conclusion of the analysis is given.

CHAPTER 2

COSMIC RAY PHENOMENOLOGY

2.1 History of Discovery of Cosmic Rays

The discovery of cosmic rays was a long process that initially started with Coulomb's discovery in 1785 of the discharge of the electroscopes [1]. In 1879, Crookes published that this discharge rate depends on the pressure in the electroscope chamber. When air pressure increases, the discharge rate also increases [5].

After 17 years, in 1896, Becquerel discovered that nuclear instability causes radioactive emission from nuclei, which was named spontaneous radioactivity. In that discovery, the electroscope discharged instantly in the presence of radioactive material. The ionization of the air from the radioactive emissions in the materials surrounding the electroscope contributed to this discharge. In 1900, the quality of the insulation of the electroscope was increased, and this enabled new experiments to be performed [6]. With that improvement, spontaneous discharge should not have happened in an insulated environment; however discharging radiation was still present even though at the time it was thought that it could not penetrate through the metal shielding.

At the time, it was known that the alpha decay had the shortest penetrating distance, and alpha particles could be stopped by paper, while for beta decay, a thin foil of aluminium was sufficient to shield them. Since radiation was present despite the metal shielding, this type of radiation could only be a gamma-ray. Three possible candidates were considered at that time as a source of this radiation. First was an extraterrestrial radioactive source, most likely our Sun, second was the radioactivity of the atmosphere, and the third was radioactive materials within the Earth's crust.

During the 1910s, Domenico Pacini, who was an Italian physicist, carried out an underwater experiment to search for evidence of the radiation that resulted from the Earth's crust [7]. Pacini made separate measurements of air ionization on the surface of the Earth and the sea. He found that the radiation on the Earth's crust and the sea was not remarkably different. As a next step, Pacini carried out experiments underwater, and in 1912 he published that there was a decrease in the number of ions detected on the surface of the sea and three meters under the water [8]. He concluded that the decrease of about 20% is not due to the radiation coming from the Earth's crust. Several other experiments also ended up with the same result. As one goes more deeper in the sea, the radiation decreases.

In the same years, balloon flight experiments were also carried out to prove that the radiation was terrestrial. Alfred Gockel, who was a professor at University of Fribourg, managed to reach an altitude of 4500m by using a balloon in 1909 [9]; however, he could not see the decrease that there should have been if the radiation was terrestrial. He confirmed the measurements of Pacini and agreed with the non-terrestrial origin of the radiation.

Figure 2.1: Victor Hess during the preparation his baloon flight in August 1912. [1]

Despite growing evidence showing that the radiation does not have a terrestrial origin,

physicists did not agree on this conclusion for a long time. Victor Hess, who was an Austrian physicist, flew seven times with a balloon between April 1912 and August 1912. He published his observations separately [10]. His last flight was in August, and he reached 5200m. The results of this flight were definitive and not expected.

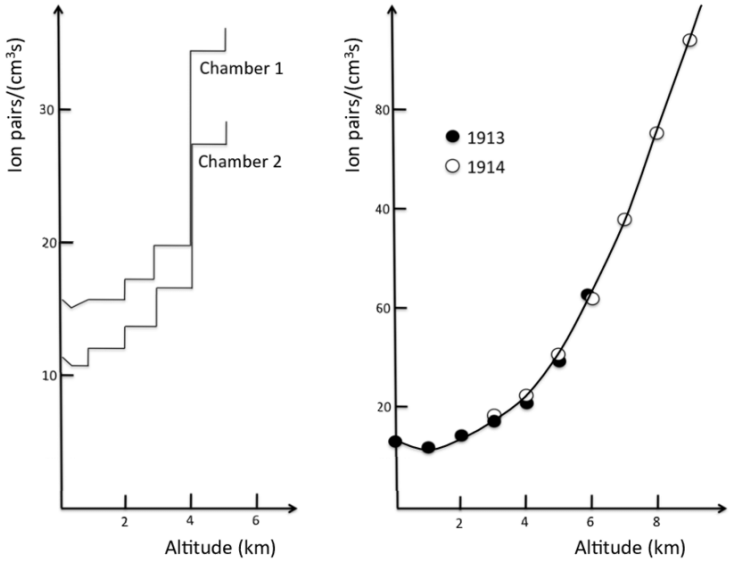

Figure 2.2: Altitude dependency of ionization. Left: Results of Hess' flight with two ion chambers. Right: Results of Kolhörster [11]

With his observations, he concluded that the increase of radiation at lower altitudes (2-4km) was less than at high altitudes (4-6km). This was a remarkable result because it proved that source of the radiation must be extraterrestrial. Kolhörster then confirmed Hess's results in 1913-1914. He, on the other hand, managed to reach an altitude of 9200m, and he found out the radiation level was ten times the ground level radiation [11].

The second step was understanding the nature of this incoming radiation from space. With the observation performed by Jacob Clay during 1926-1927, it appeared that ionization from cosmic rays also depends on latitude. He found that the measured flux changes depending on the latitude with the data taken in Amsterdam and in the Dutch East Indies [12]. He concluded that the amount of ionization increases with the increasing latitude, which implies that cosmic rays are interacting with the Earth's geomagnetic field.

Stormer, in 1955, theorized that the motion of charged particles in the Earth's magnetic field can be determined by 2.5.1. By assuming that the magnetic field of the Earth can be approximated as a dipole field, Stormer was able to express [13] a geomagnetic cutoff rigidity, R_c (which will be explained later) that describes the minimum amount of rigidity that a particle should have to reach a particular altitude. R_c can be expressed as in equation 2.5.1 where R_c is the geomagnetic cutoff rigidity in MV, *M* is the magnitude of the Earth's dipole moment in Gcm^3, λ is the latitude from the magnetic equator, ϵ is the angle from the radial direction with respect to position of the center of the dipole, or in other words from the zenith angle, *r* is the distance from the center of the dipole and finally ξ is the azimuthal angle in clockwise direction from the North magnetic pole [14]:

$$\mathbf{R}_c = \frac{M.cos^4\lambda}{r^2[1 + (1 - sin\epsilon.sin\xi.cos^3\lambda)^{1/2}]^2} \tag{2.1.1}$$

In the meanwhile, in 1949, Fermi found an acceleration mechanism which is called by his name today, Fermi mechanism or diffusive shock mechanism which explains how the charged particles are accelerated by magnetic mirroring [15]. With that discovery, the production, acceleration and propagation mechanisms of cosmic rays were understood better.

Today, rather than contributions by individual scientists, many cosmic ray experiments, space-based or ground-based experiments, are carried by groups of people in a large collaboration, enabling the construction of complicated experiments and using different detectors with advanced designs and high precision. Space-based experiments such as Fermi Gamma-Ray Space Telescope (FGST), Payload for Antimatter Matter Exploration and Light-nuclei Astrophysics (PAMELA) and AMS-02 are experiments that gave remarkable results about cosmic ray acceleration and propagation as well as dark matter and antimatter researches. Ground-based experiments such as H.E.S.S, MAGIC, and VERITAS are measuring cosmic rays indirectly after interacting in the Earth's atmosphere [1].

2.2 Acceleration Mechanism for Cosmic Rays

After understanding that cosmic rays cause the increase of radioactivity in the Earth's atmosphere, the second step was understanding the origin, acceleration and propagation mechanisms of cosmic rays. Fermi mechanism describes how charged cosmic rays gain energy during diffusive shock acceleration in a collisionless medium. For the Fermi mechanism to be valid, the medium must be collisionless since it includes non-thermal particles. Fermi mechanism also explains the observed power-law energy spectrum for charged cosmic rays.

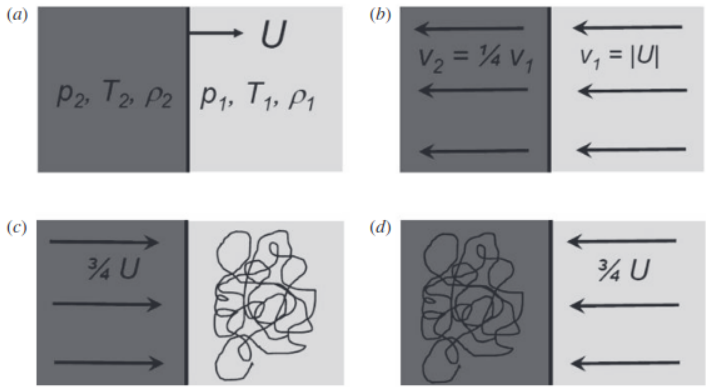

Figure 2.3: Fermi Mechanism Fermi mechanism as observed in different frames. A shock wave with speed U is propagating in a stationary gas through two regions called a upstream region with density ρ_1, pressure p_1 and temperature T_1 and a downstream region with density ρ_2, pressure p_2 and temperature T_2. [16]

Figure 2.3 gives an illustration of how the Fermi mechanism works. A shock wave that has a velocity U is propagating in stationary gas through two regions called downstream and upstream. The downstream region is the one behind the shock wave, and the upstream region is the one ahead of the shock frame. The gas density, pressure and temperature in the downstream region are ρ_2, p_2 and T_2 respectively. In the upstream region, they are defined as ρ_1, p_1 and T_1 . Picture (a) is called the lab frame.

In the shock frame picture, the shock wave is considered as stationary and the upstream gas moves towards the shock with velocity v_1 and the downstream region moves away from the shock with velocity v_2 which is $v_2 = \frac{1}{4} v_1$ as shown in figure (b). Considering the strong shock, the densities of these two mediums are related via

equation 2.2.1:

$$\frac{\rho_1}{\rho_2} = \frac{\gamma - 1}{\gamma + 1} \tag{2.2.1}$$

For mono-atomic or fully ionized gas, γ factor equals to $\frac{5}{3}$, from the energy conservation of gas dynamics where γ is $\frac{c_p}{c_v}$, specific heat capacities. From the continuity equation, two mediums are related by 2.2.2 :

$$\rho_1 v_1 = \rho_2 v_2 \tag{2.2.2}$$

Using these two equations 2.2.1 and 2.2.2 v_2 can be written as:

$$v_2 = \frac{1}{4} v_1 \tag{2.2.3}$$

So for shock the frame, the upstream region with velocity v_1 which is equal to U and the downstream region with velocity v_2= $\frac{1}{4}$ v_1. Now considering the upstream frame, in figure (c), the downstream gas has a velocity $\frac{3}{4} v_1$ and finally, in the downstream frame, the upstream region has a velocity $\frac{3}{4} v_1$. Since the particles are moving within the medium, the velocities are also valid for the particles' reference frame. So there is a relative velocity V = $\frac{3}{4} v_1$ between these two regions and also the particles in these regions.

The energy gain of particles for one full round then can be calculated. Consider a particle in the upstream region with energy E and momentum p. Let observed energy and momentum in the downstream frame be E' and p' where

$$E' = \Gamma[E + V p_x] \tag{2.2.4}$$

Since the non-relativistic shock has $\Gamma \sim 1$ then equation 2.2.4 becomes:

$$E' - E = V p_x \tag{2.2.5}$$

The θ is the angle between the direction of propagation of shock wave, which is namely x-axis and the incoming particle and with p_x = $pcos\theta$ and since the particles are relativistic $p = \frac{E}{c}$, one can write equation 2.2.5 as :

$$\frac{\Delta E}{E} = \frac{V}{c} cos\theta \tag{2.2.6}$$

The probability that the incoming particle will diffuse into the shock wave through the volume between θ and $\theta + d\theta$ is proportional to $sin\theta d\theta$. Also the rate at which the particles come towards to the shock wave is proportional to the x-component of their velocities, $cos\theta$. If one only considers only the first quarter of the shock approaching, then by normalizing the integral 2.2.7

$$\int_0^{\pi/2} cos\theta sin\theta d\theta \tag{2.2.7}$$

the probability distribution of approaching particles become

$$p(\theta) = 2sin\theta cos\theta \tag{2.2.8}$$

and the average energy gain while crossing the shock from one side to other is

$$< \frac{\Delta E}{E} >= \frac{V}{c} \int_0^{\pi/2} 2cos^2\theta sin\theta d\theta \tag{2.2.9}$$

and therefore

$$< \frac{\Delta E}{E} >= \frac{2}{3}\frac{V}{c} \tag{2.2.10}$$

Since the collisions are head-on collisions, the energy gained per interaction is proportional to the first power, equation 2.2.10 is called the *First Order Fermi Mechanism*. Equation 2.2.10 can also be written as

$$\beta = \frac{E'}{E} = 1 + \frac{V}{c} cos\theta. \tag{2.2.11}$$

The number of particles diffuse in the shock wave at a rate of $\frac{1}{4}Nc$ in the upstream frame and the particles' gain in the downstream frame is NV. The gain and loss must be equal, so $NV = \frac{1}{4}Nc$ .Then the ratio of these two rates is $\frac{U}{c}$. Therefore, the escape probability of the particles $P = 1 - U/c$. Hence the diffusion loss equation is given by 2.2.12

$$N(E)dE = CE^{-1+lnP/ln\beta}dE \tag{2.2.12}$$

where C is constant. By taking the expansion up to first order in $lnP = ln(1 - \frac{U}{c}) \cong -\frac{U}{c}$ and with the help of equation 2.2.9 one can see that

$$N(E)dE \propto E^{-2}dE \tag{2.2.13}$$

which is also called as *differential energy spectrum* and illustrates an approach to the power law behaviour of cosmic ray energy spectrum[16]. However, the interaction of the accelerated particles with the surrounding environment can cause a steepening in the spectrum [17].

2.3 Propagation, Energy Spectrum and Composition of Cosmic Rays

The charged cosmic ray particles propagate by diffusion in magnetic a field and the power-law behaviour of cosmic ray fluxes measured by various experiments including AMS-02 can be seen in figure 2.4.

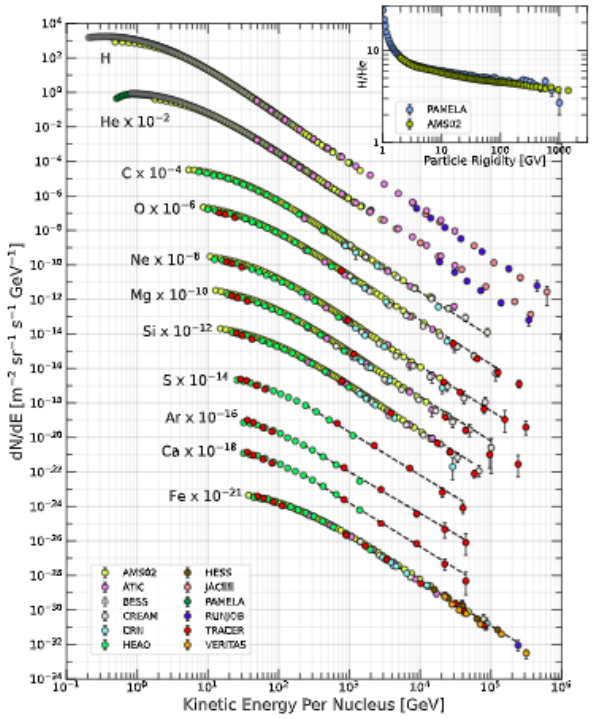

Figure 2.4: Cosmic rays energy spectrum from 100 MeV to 10^6 GeV showing various nuclei, with x axis representing the kinetic energy per nucleus in GeV and y axis representing the fluxes of nuclei of energy-per-nucleus [18]

This spectrum can be separated into three main regions; low energy region that is below 1 GeV and the effect of geomagnetic cutoff of the Earth can easily be seen, the galactic cosmic ray region, which is between a one GeV and $\sim 10^9$ GeV and extragalactic cosmic ray region which is above 10^9 GeV [19]. In figure 2.5 we see three main characteristics of cosmic ray spectrum. The first one is called the *knee* around 10^6 GeV, which is changes in the slope where it becomes steeper and the second feature is called the *ankle* where spectrum exhibits a flattening around 10^9GeV and the third one is called the *Greisen- Zatsepin-Kuzmin (GZK) cut-off* , reason of which is explained in section 2.3.3, which is around 10^{11}GeV.

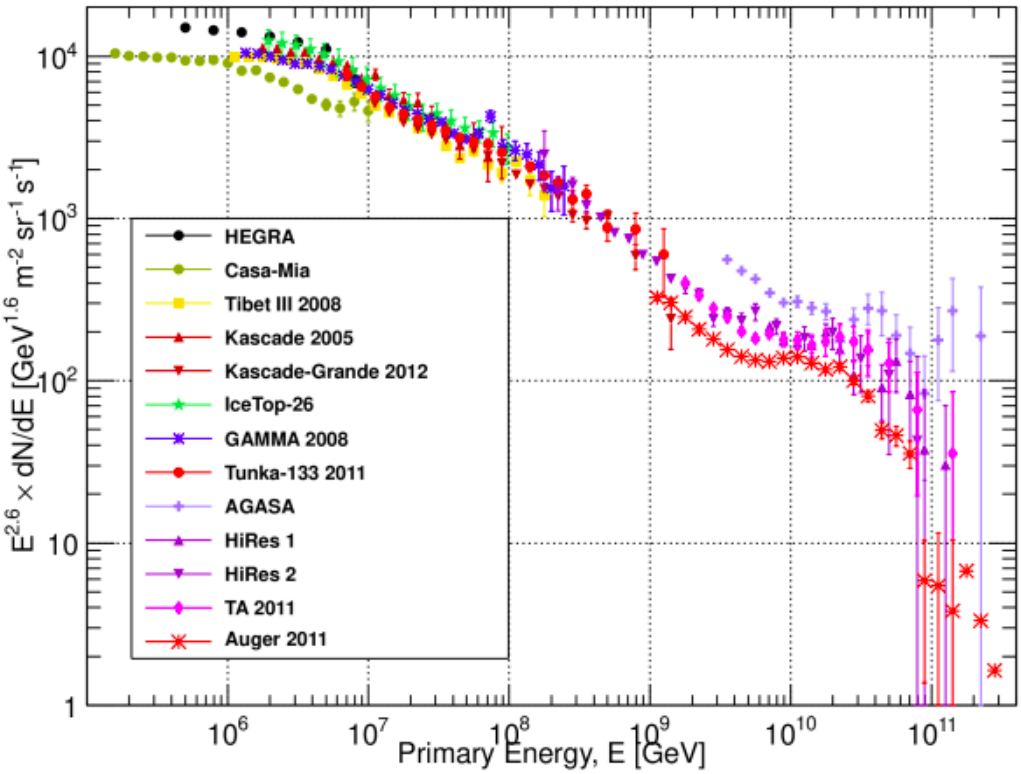

Figure 2.5: Energy spectrum for cosmic rays from 10^6 GeV to 10^{11} GeV from various cosmic ray air shower experiments multiplied by spectral index. The x axis shows the primary energy per experiment in GeV and the y axis shows the flux multiplied by the energy to the spectral index. [2]

Figure 2.5 shows cosmic ray energy spectrum as multiplied by $E^{2.6}$ so that it is easier to see the changes in the slope measured by various air shower experiments. The *Knee*, the *ankle* and the *GZK cut-off* can be seen easily in that case.

2.3.1 Low Energetic Cosmic Rays

Low energetic cosmic ray region is below $\sim$ 1GeV in which the main source for the CR is *solar energetic particles (SEP)* emitted from our Sun by either *flares* or *Coronal Mass Ejection (CME)* [20]. In the region below 1 GeV, there is a decrease in the flux, which can be seen in figure 2.4. This is thought to be due to the magnetic field of the Sun and the Earth. On the other hand, detected SEPs have a feature that

is time-dependent, which is called solar modulation. There are 22-years and 11-years of solar cycle as well as 27, 13.5, 9 days of periodicities. When the Sun is at its solar maximum, the rate of ejections increase, which result in a decrease in the flux of galactic cosmic rays and an increase in the flux of solar cosmic rays. When it is at its solar minimum, the opposite occurs [21].

2.3.1.1 Forbush Decrease and Periodic Variations of the Sun

The decrease in the galactic cosmic ray flux near the Earth can be explained by the Forbush decrease. As mentioned in previous section, the increase in the flux emitted by the Sun causes a reduction in the amount of galactic cosmic ray flux observed on the near Earth. Forbush decrease can be caused by two main reasons, which are *coronal mass ejections* and the shock waves created by the interaction of a high-speed solar wind with the solar wind which has a slower speed. According to the magnitude of the Forbush decrease effect, it can disturb the geomagnetic field of the Earth. This amount of disturbance can be denoted by an index the so-called *planetary K index* or, in other words, K_p index [22]. The K_p index, which ranges from 1 to 9, is a measure of the variation from a "calm day curve". Depending on the magnitude of the K_p index, it is possible to understand the activity level of the Sun. The change in the activity of the Sun causes a disturbance in the magnetosphere-ionosphere of the Earth and this activity changes are called *geoeffective processes*. 11-year and 22-year cycles are well-known consequences of these changes; however, these are not the only significant changes.

The change in the solar CR flux as observed from the Earth strongly depends on the motion of the Earth and the rotation of the Sun on its own axis. The Earth-Sun system has two movements, one of which is the *sideral motion* that is the period required for the Earth to complete 360° rotation around itself and the other one is the *synodic motion* that is the period required for the Sun to return the same position as it appears on the Earth. Synodic motion is the main reason for the 27-day periodicity, called Bartel rotation, that the flux emitted by the Sun exhibits. The reason that the synodic motion causes such a disturbance is the inhomogeneity of the plasma of the Sun, but it should be noted that the rotation rate of the Sun changes depending on its helio-

graphic latitude. The rotation rate of the gaseous plasma composition of the Sun is the fastest at the equator, and it decreases towards the poles. The variables that characterize the solar wind such as density, velocity and Interplanetary Magnetic Field (IMF) intensity can also be used to detect a 27-day periodicity. Since the change in the magnetic field density near the Earth results from the interaction between the IMF and the geomagnetic field, it is crucial to understand the magnetic field components of coherent solar wind.

High-speed streams (HSS) are emitted from coronal holes close to the Sun's equator. When these streams interact with the slower ones, a compressed plasma region that is called a corotating interaction region (CIR) are formed due to the spin given to the streams by the Sun. The coronal holes usually live more than months. The 27-days periodicity is affected by these HSS and the 13.5-day and 9-day periodicities are thought to be created by "multiple coronal holes" that are located near the equatorial [23].

2.3.2 Galactic Cosmic Rays (GCRs)

In the region between one GeV and 10^9 GeV, CRs are thought to be originating from our galaxy, the Milky Way. *Supernova Remnants (SNRs)* are the primary source for the production of CR at high energies.

When the atomic number is increased, the energy at which the knee appeares is also increased [24]. Knee occurs at an energy between 2 to 4 x 10^6 times of the rest mass of the nuclei [25].

2.3.3 Extra Galactic Cosmic Rays

Cosmic rays above $\sim 10^9$ GeV are called extragalactic cosmic rays or in other words *Ultra High Energetic Cosmic Rays (UHECRs).* They are mainly proton and nuclei accelerated in astrophysical sources outside the galaxy. After $\sim 10^9$ GeV, the strength of the magnetic field of the galaxy is not enough to bend even the heaviest nuclei, which results in nuclei leakage and therefore, the detected UHECR nuclei must be

extragalactic [26]. The GZK cut-off around 10^{11} GeV can be explained by when the energy of the γ in the proton rest frame exceeds the mass of the π^+ for the following interaction 2.3.1

$$p + \gamma \longrightarrow n + \pi^+ \tag{2.3.1}$$

where the photons have energy $\sim 10^{-4}$ eV with CMBR temperature 3K, the result is 10^{20} eV, the threshold energy results in $\sim 10^{20}$ eV (10^{11} GeV) . That means any CRs which have more than this amount of energy will interact with the CMBR photons [27].

GCRs, all of which are charged nuclei, are composed of 87% of protons, 12% of He and 1% of heavier nuclei. Depending on the source, whether the particle is SEP or belongs to GCRs / UHECRs, the abundances of the nuclei in CR changes.

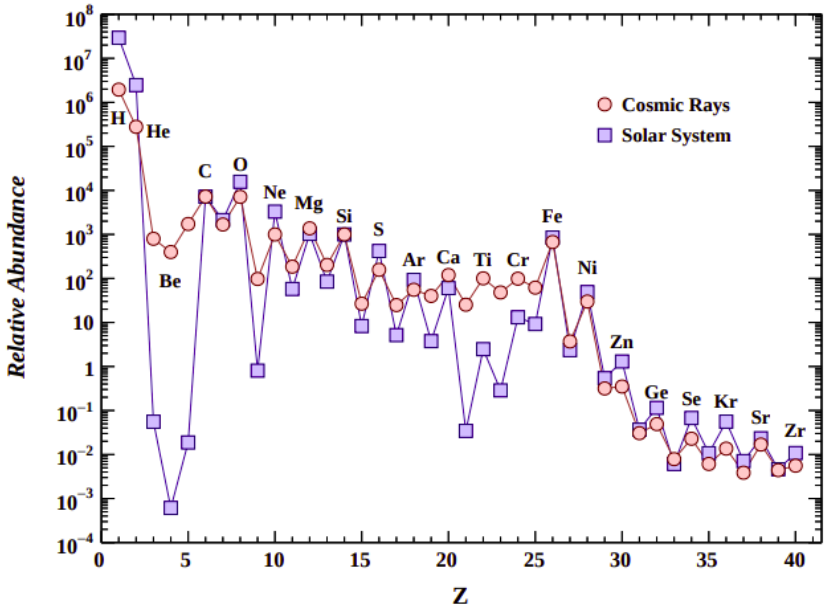

Figure 2.6: Relative abundance of nuclei in CR composition and the Solar System presented by Particle Data Group. Primary nuclei such as H and He are more abundant in the solar system while secondary nuclei such as Li, Be and B are less abundant in the solar system [18].

Figure 2.6 shows the relative abundances of nuclei. From the figure, one can realize that for some nuclei, such as, Li, Be, B, the abundance is very different in two sit-

uations. Primary cosmic rays are the ones created in the astrophysical sources; and secondary particles, on the other hand, are created or destroyed as a result of the interaction of primaries with Interstellar Medium (ISM). So nuclei like H, He, C, O are examples of primaries and Li, Be, B are examples of secondaries [28]. Secondary particles which have odd-even number relation become more stable with interacting protons coming from the Sun. Therefore the abundance of secondaries are lower in the solar system abundance. Even though Be has a even-even number relation, due to the extreme tight binding of He nuclei, it has a high tendency of alpha decay and exhibits an instability.

2.4 Detection of Cosmic Rays

There are different phenomena used to detect charged cosmic ray particles. Most of the time, experiments combine different types of detection methods together to have a more precise measurement. For example observing the time of flight or the Cherenkov angle of a particle, one can determine the velocity of a charged particle. The total energy of a particle can be measured by calorimeters. Finally, the energy loss of a charged particle in unit length x can be found by the following formula [29] :

$$-\frac{dE}{dx} = Kz^2\rho\frac{Z}{A}\frac{1}{\beta^2}\left[ln\left(\frac{2m_ec^2\beta^2\gamma^2}{I}\right) - \beta^2\right] \tag{2.4.1}$$

Equation 2.4.1 is called Bethe-Bloch formula where constant K is $4\pi N_A r_e^2 m_e c^2$ which equals to 0.307 $MeVcm^2mol^{-1}$, N_A is Avagadro's number, r_e is electron radius, m_e is electron mass, M is mass of the projectile in MeV, z is charge of the projectile in units of e, Z is the atomic number and A (in $gmol^{-1}$) is the mass number of absorber. I is the mean excitation energy in MeV and finally ρ is the density of absorber material in gcm^{-1}. As usual, $\beta \equiv v/c$ and $\gamma \equiv (1-\beta^2)^{-\frac{1}{2}}$. From equation 2.4.1, it can be seen that the energy loss of a charged particle in unit length x is proportional with Q^2. Charged particles with a certain energy can pass through a material leaving minimal energy. These particles are called minimum ionization particles (MIPs). If the $\beta\gamma$ of the a single charged particle is around 3, this particle is

considered to be a MIP and will leave around $2MeVcm^2/gr$ (PDG REFERANS).

Ionization is one of the first principles utilized to detect charged particles. For example in a gaseous particle detector, when a particle passes through the gas, it ionizes the gas that it passes through. A particle with enough energy can ionize the gas and create electron-ion pairs which results in a current flow which can be measured.

The second way of detection is the one in scintillation detectors. When a charged particle passes through a scintillation detector, it causes an emissions of photons called scintillation. That signal is converted into an electrical signal with the help of photomultipliers.

The third one is a principle called *Cherenkov Radiation*. This principle states that, when a charged particle with velocity v enters a medium with index n, it emits a radiation if that particles' velocity $v > \frac{c}{n}$ where c is the speed of light.

Another type of detection is using the *Transition Radiation.* This radiation is emitted by a charged particle only if it's γ is greater than 1000 and when it passes through two mediums with different indexes.

The last one is calorimeters, whose main purpose is to cause particles t shower using heavy materials and estimate the energy of the primary particle from those measured in the shower. These methods will be discussed in detail later.

With higher energy bins of CR, the flux falls, which means that the counts of particle hits in a detector area decreases. So if one wants to detect a high energy CR, either a wide area detector is required or the time duration of the experiment should be long enough to collect enough statistics.

There are many ground-based experiments that observe high energy CRs. These experiments can contain arrays or telescopes. Figure 2.7 shows different ways of detection such as measurement of Cherenkov light and low energy muons with scintillation counters. Ground-based experiments measure CRs that shower in the atmosphere. Direct measurement of a CR is only possible above the Earth's atmosphere because when a high energy CR collides with a nucleus in the atmosphere of the Earth and it produces many other energetic particles that are called *extensive air showers* [30].

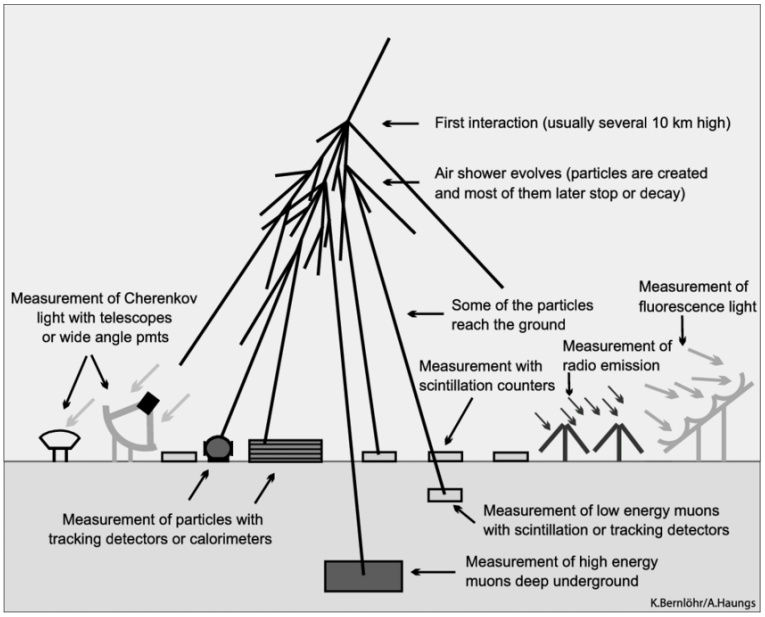

Figure 2.7: Various methods, such as detection of Cherenkov light, particle measurement with tracking detectors or calorimeters, measurement of low and high energy muons, to detect extensive air showers. [31]

Space-based or satellite-based experiments, on the other hand, are capable of measuring CRs directly. Due to mass and geometry limitations of payload-lifting space-rockets and the limited lifetime of the satellites in orbit due to space radiation and other environmental factors and therefore limited statistics, space experiments cannot measure UHECR [32].

2.5 Space Environment

In the space environment, the magnetic field of the Earth has a huge role in the movement of charged particles in the magnetosphere. There are two main phenomena that one should take into account very carefully. These effects are *Geomagnetic Cutoff* and *South Atlantic Anomaly (SAA)*.

2.5.1 Geomagnetic Cutoff

Störmer, as mentioned previously, approximated the magnetic field of the Earth as a magnetic dipole. With that assumption, he has defined a boundary for particles which is defined by the equation 2.5.1

$$\mathbf{R}_c = \frac{M.cos^4\lambda}{r^2[1+(1-sin\epsilon.sin\xi.cos^3\lambda)^{1/2}]^2} \tag{2.5.1}$$

as explained in equation 2.1.1. For each coordinate on the Earth, there is a geomagnetic rigidity value, and for a particle to reach that particular location and such a particle must have a momentum value $RZ \geq p$. The minimum amount of rigidity that a particle must have to be detected at that coordinate is called *geomagnetic cutoff rigidity* [33].

2.5.2 South Atlantic Anomaly (SAA)

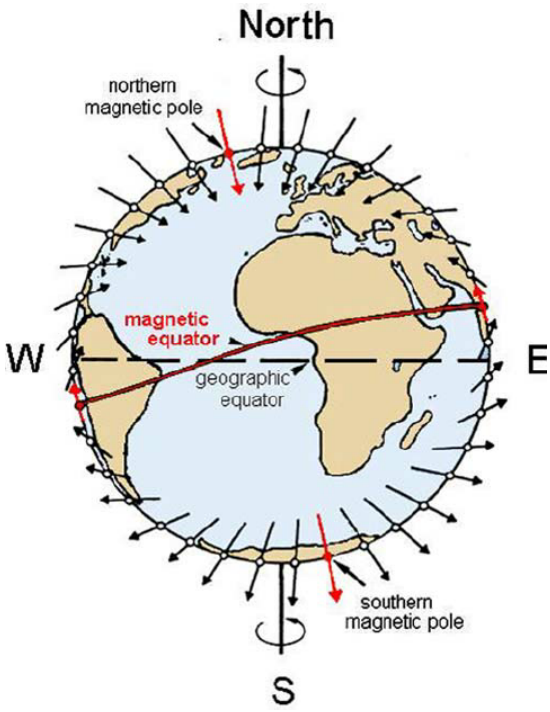

Figure 2.8: The $11.5°$ inclination of the geographic North pole of the Earth from the magnetic North pole of the Earth represented by the red arrows. [34]

Figure 2.8 shows the magnetic field of the Earth is tilted from the rotation axis of Earth with an angle of 11.5°. This creates an inhomogeneity in the magnetic field, which results in a well known effect, called the South Atlantic Anomaly (SAA).

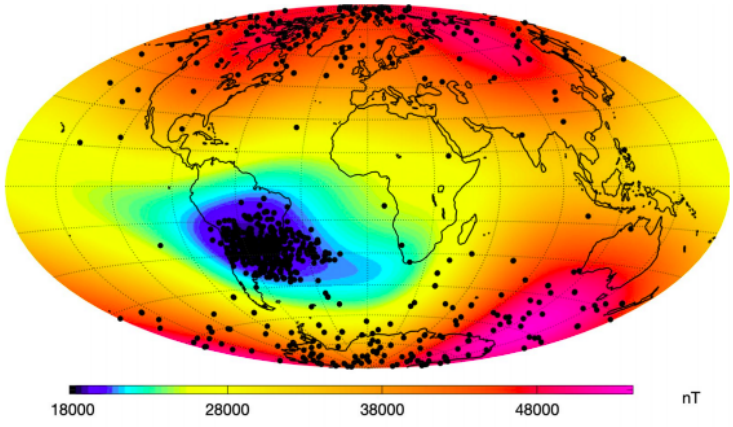

Figure 2.9: The SAA region and the single event upsets represented by black dots by Swarm satellites at an altitude 450km. The SAA region is represented in darker blue and in the magnetic field strength in nT for various locations in the bottom bar. [35]

Charged particles interact with the magnetic field of the Earth through the Lorentz force, and they accumulate in some regions, which are called the Van Allen Belts. Figure 2.9 shows the magnetic field inhomogeneity. The Blue region represents SAA. In that region, the Van Allen Belts come closest to the surface of the Earth, which also means in that particular region flux is higher than the other areas since the strength of the magnetic field which protects the Earth from the radiation is weaker. Satellites that pass through that region need to have operational precaution in place [36]. Since International Space Station (ISS) also passes in that region, this effect must be considered while performing the analysis with AMS-02.

CHAPTER 3

ALPHA MAGNETIC SPECTROMETER (AMS-02)

3.1 AMS-02

AMS-02 is a particle physics experiment that can perform precision measurements with a large acceptance for cosmic rays. It was installed on the International Space Station (ISS) in May 2011. ISS moves from the West to the East and has an orbital inclination of 51.6 degrees. It's altitude varies between 418-422km. It will continue its operations while it is supported on the ISS, which is almost 20 years in total. Until January 2022, AMS-02 has collected 197 billion events [37].

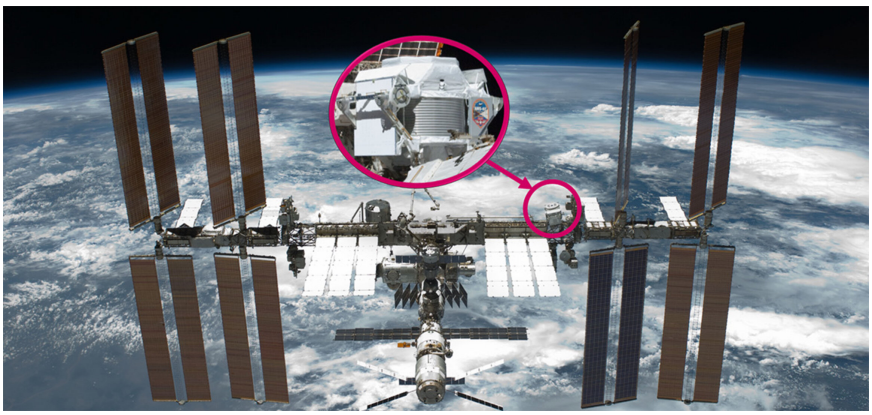

Figure 3.1: AMS-02 on the International Space Station launched in 16^{th} of May 2011, orbiting around the Earth [38]

AMS-02 has several physics purposes to research. It collects data to understand for the origin, acceleration and propagation of CR and searches for anti-matter and dark matter. AMS-02 is an experiment that consists of many sub-detectors which have different functionalities. Figure 3.2 shows the subdetectors of AMS-02. From top

to bottom, the Silicon Tracker is located between the Transition Radiation Detector(TRD), followed by the layers of Time of Flight(ToF). The ST is surrounded by a permanent magnet that curves charged particle tracks. After the lower layers of ToF, the Rich Image Cherenkov Detector (RICH) follows. The last layer of ST is located between the RICH and the Electromagnetic Calorimeter (ECAL).

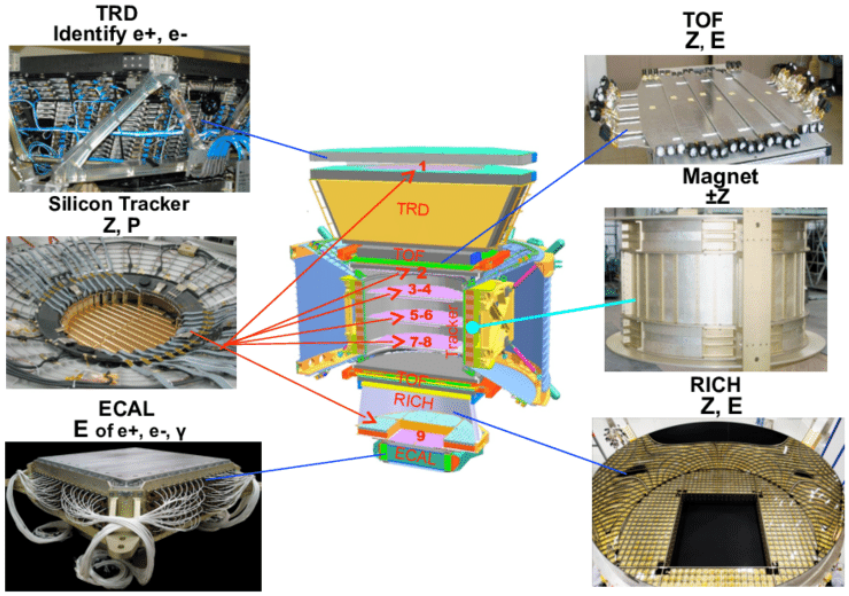

Figure 3.2: Cut-away view of AMS-02 that photos of each subdetector that the TRD distinguishing positrons and electrons, the ToF measuring the charge and the energy of the particle, the silicon tracker measuring charge and the momentum of the particle, the RICH measuring the charge and the energy of the particle, the ECAL detecting photons and measuring the energy as well as distinguish positrons and electrons, and the magnet producing a magnetic field of 0.15T. [39]

The permanent magnet produces a magnetic field in the x-direction and the symmetry axis of the detector is the z-axis. AMS-02 triggers the up-going particles and the particles that are coming side-ways. The data flow of AMS-02 has several stages. To begin with, AMS-02 collects trigerred events which are stored in the laptop on the ISS. From there, the data is transmitted, with an average of rate 10Mbit/s to one of three Tracking and Data Relay Satellites (TRDS) and then to White Sands Ground Terminal in New Mexico. After that point, the data flow takes place on the ground.

From White Sands Ground Terminal, the data is referred to Marshall Space Flight Center, and it is written on disk, stored and transferred to Payload Operations and Control Center (POCC) located at CERN, in Geneva. In the POCC, scientists take shifts 24 hours per days to check the data flow and control the operations of the subdetectors such as adjusting the gain of pre-amplifiers on readout electronics. If any system warning or error occurs, the shift leader is informed immediately.

Figure 3.3: AMS POCC at CERN close to Geneva. In the middle screen the orbit of ISS is being followed live. Shift takers and experts in different desks watch different systems such as thermal system, data acquisition and the operation of spesific sub-detectors [37]

The shift takers in the POCC also carefully monitor the variations in thermal conditions of AMS, which is affected by a number of parameters. The first parameter is called the *solar beta angle* β. Figure 3.4 illustrates the β angle. It is defined as the angle between the orbital plane of the ISS and the direction vector from the Sun to the Earth. As β changes, depending on its value, certain parts of the AMS-02 detector can get very cold or very hot. Another parameter is called the *solar constant*. It is defined as the illumination power of the Sun. As opposed to its name, the solar constant is not

actually a constant, and it varies between 1326 W/m^2 - 1418 W/m^2 depending on the mean Earth-Sun distance. The last two parameters that affect thermal conditions of AMS are the infrared Earth radiation and the albedo level of Earth, which can also be thought of as the amount of reflected Sunlight. In order to be able to monitor the temperature changes in detail, AMS has more than 1100 temperature sensors and almost 300 heaters which are constantly being controlled in the POCC. Any temperature that exceeds operational limits may cause long term damage in AMS-02 electronics [40].

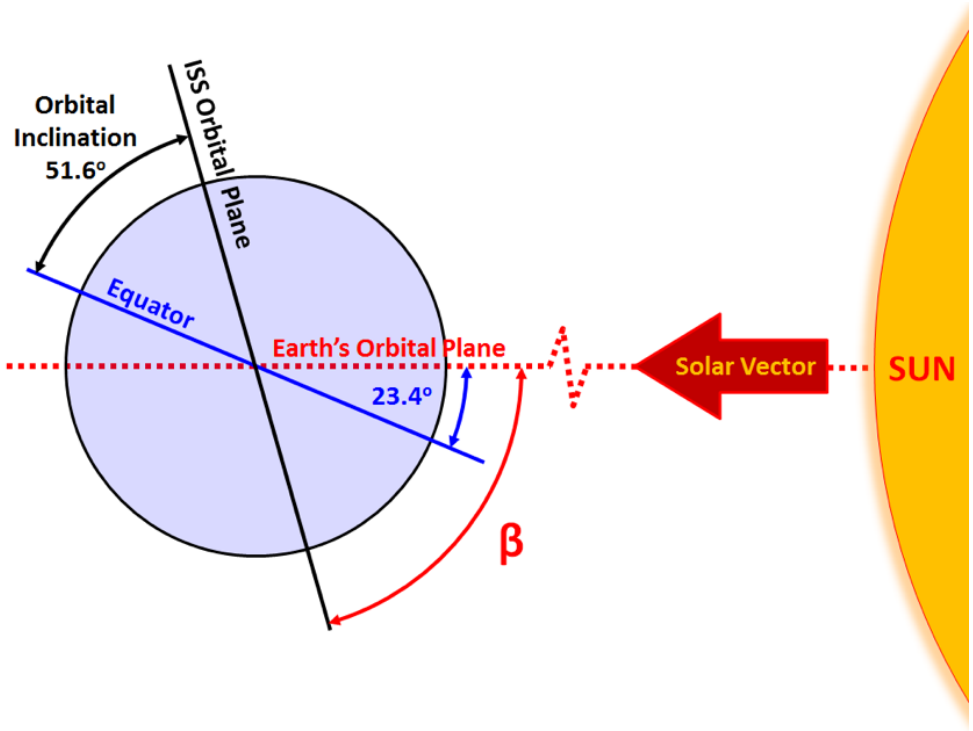

Figure 3.4: Solar Beta Angle between the ISS orbital plane and the Earth's orbital plane in the direction of solar vector [40]

3.2 Subdetectors of AMS-02

As mentioned in the previous section, AMS-02 has five subdetectors which are the ToF, ST, TRD, RICH and the ECAL. ST is surrounded by a permanent magnet which creates a magnetic field with a magnitude of 0.15T in the x-direction. Each of these subdetectors has different functionalities, and measure the quantities denoted in the figure. A particle that traverses of all AMS will be measured several times using

different physics principles which gives an opportunity to cross-check the numerical values.

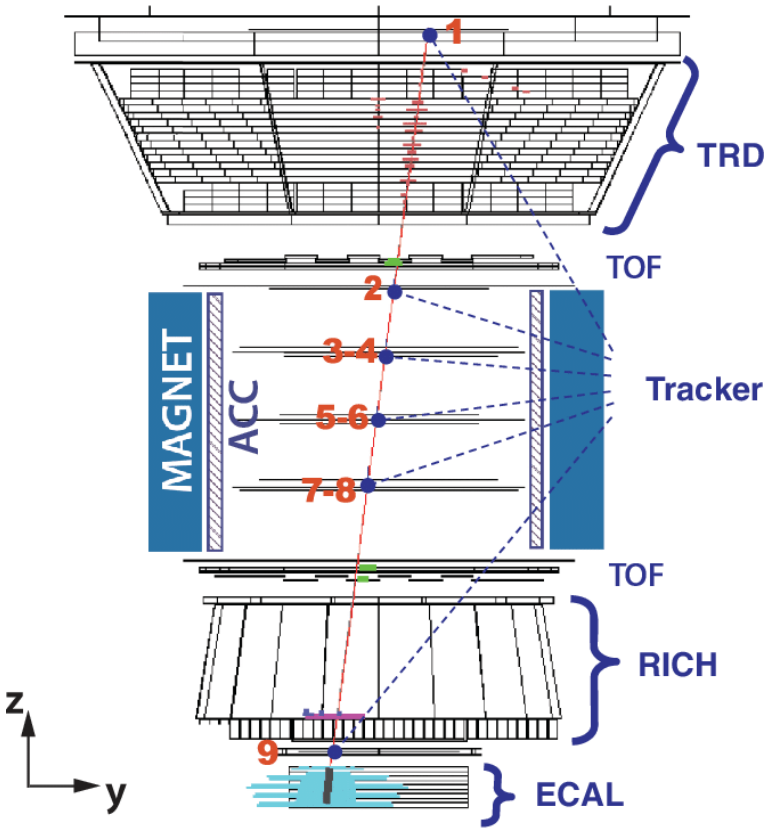

Figure 3.5: An event display inside the AMS. A particle hits the layer 1, goes through the TRD, hits all the inner layers as well as upper and lower ToF and finally reaches the ECAL. [41]

3.2.1 Time of Flight (ToF) Detector

ToF detector measures both the charge through the dE/dx measurement in the scintillator through the time difference of the signals in the scintillators and the flight time of the particle. ToF detector consists of four layers of plastic scintillator counters, two of which are located between the TRD and Layer 2 of the ST are called the *Upper ToF*, and the other two are located between the magnet and the RICH are called *Lower ToF*.

Four ToF layers have (8x8) and (10x8) paddles with different lengths and each paddle

is connected to a *PhotoMultiplier Tube (PMT)* which in total makes 144 PMTs [42]. The ToF is also used as a fast trigger for the experiment, thanks to its fast response rate. By measuring the flight time and the velocity, the direction of the particle can be calculated therefore, the ToF can distinguish particles that are coming from the bottom of the detector, namely up-going and the particles that are coming from above of the detector, the so-called down-going particles. By measuring charge, the ToF can distinguish the heavy ion components of CRs.

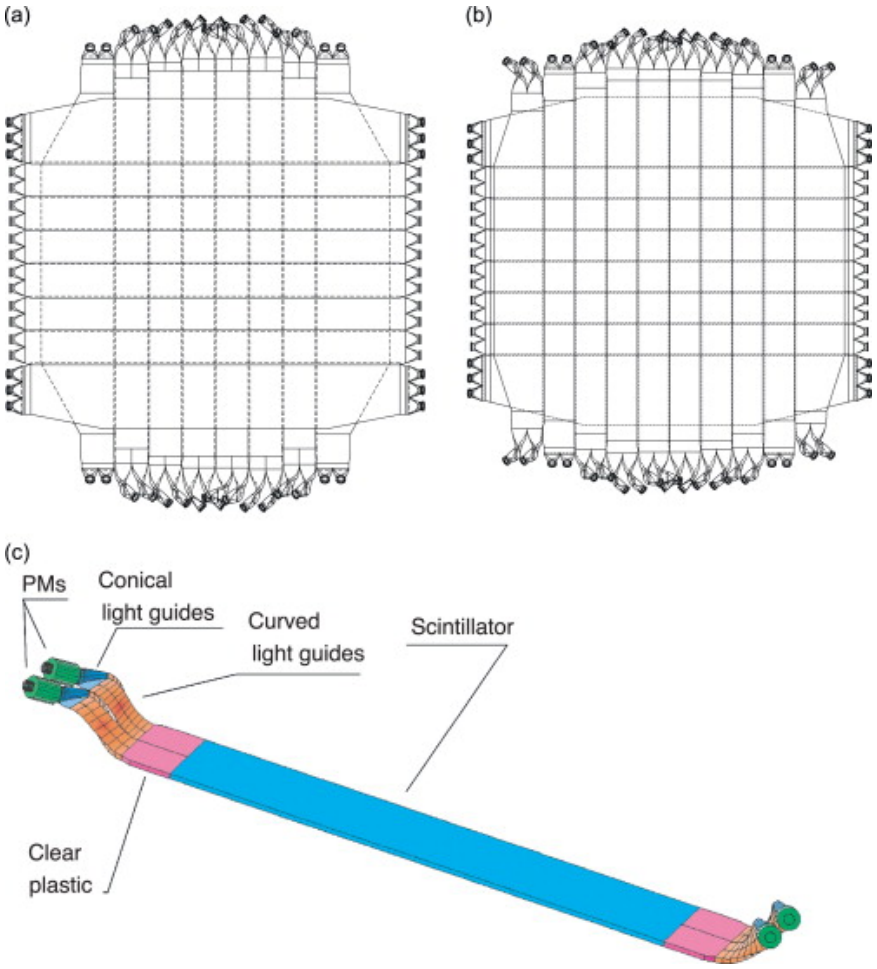

Figure 3.6: The AMS ToF Detector; (a) Upper ToF Plane, (b) Lower ToF Plane, (c) one whole counter with PMs at the both ends that are attached to conical light guides and curved light guides [43].

Figure 4.5 shows the ToF detector, the upper(a) and the lower(b) ToF planes along with a scintillator with photomultipliers on both ends. The photomultiplier readout can be easily seen at the end of each scintillator counter, which is 1cm thick plastic

scintillator [43]. The purpose of the PMT is to produce a large and proportional output signal from the detected photons using the photoelectric effect and electron multiplication in ladders of increasing potential.

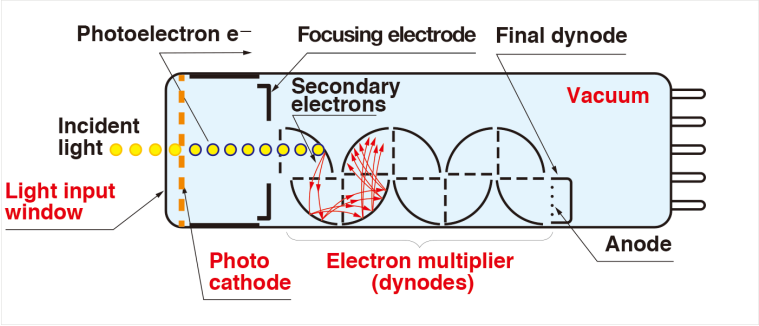

Figure 3.7: Layout of a Hamamatsu PMT and a display of the photo multiplication process in the PMT [**?**]

Figure 3.7 shows the layout of a PMT. The PMT consists of many parts such as an input window where the light enters, a photocathode where electrons are released by the photoelectric effect and moves into focusing electrodes, in which they are accelerated and focused. Then, the electrons reach dynodes or, in other words, electron multipliers where they are multiplied by secondary electron emission, and finally, they reach the anode and are collected by it [44]. The PMT anode and the third last dynode signals are readout independently. The 95% of the anode signal is employed for the time measurement and the trigger and subjected to three thresholds, which are a *Low Threshold (LT)* that is set at $\sim$ 20% of minimum ionization proton (MIP) signal, a *High Threshold (HT)* which provides a trigger for particles with $Z \geq 1$ and set at $\sim$ 60% of MIP and a *Super High Threshold (SHT)* which is responsible for triggering particles with $Z \geq 2$ and set at $\sim$ 400%. When a signal is over these thresholds, it is assigned as an output and sent to a High Performance Time to Digital Converter to record the time. The rest 5% of the anode signal is used for the detection of absolute charge with $1 \leq |Z| \leq 8$. When anode signal is supported by the dynode signal, particles with charge $|Z| \geq 3$ can also be distinguished [43].

3.2.2 Transition Radiation Detector (TRD)

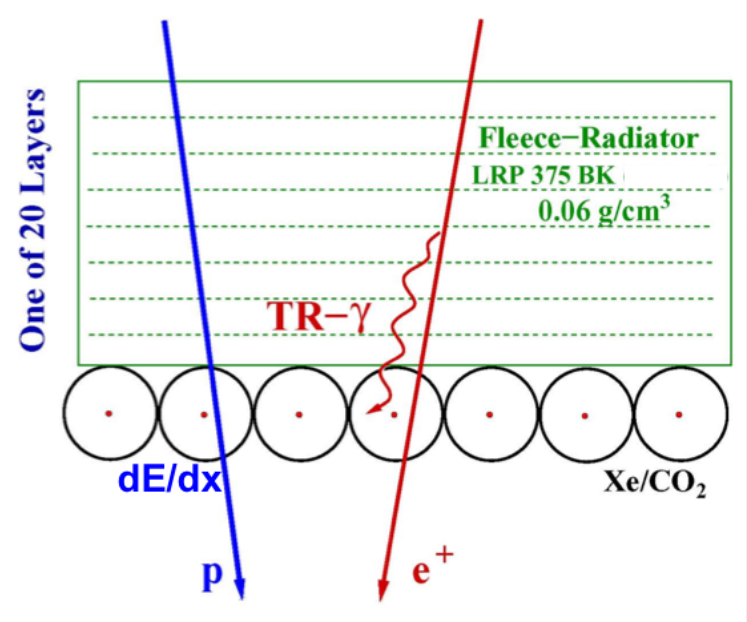

(a) A TR photon is not emitted when a proton passes through the radiators of the TRD (left) while a TR photon is emitted when a positron passes through it (right) and deposits extra energy into the proportional gas tubes of the TRD besides the energy loss of the original particle. *[45]*

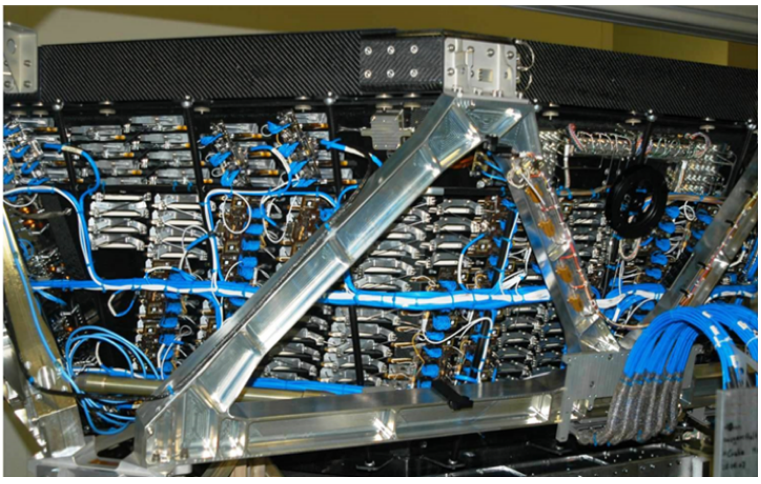

(b) A picture of the AMS TRD where the white layers of the TRD can be seen as well as the readout electronics straw tubes

Transition Radiation Detector (TRD) is mainly responsible for the separation of positrons from protons and therefore, the TRD's is separation is an essential tool for searching the dark matter, which is one of the physics objectives of AMS-02. TRD is capable of distinguishing anti-protons and positrons by rejecting their respective backgrounds namely electrons and protons by a factor of 10^2 to 10^3 in the energy range 10 to 300 GeV. In this range, the lighter the particles are, the higher the probability that they will emit *Transition Radiation (TR)* photons. As the principle is mentioned in section 2.4, a TR photon is emitted when a charged particle, whose speed is very close to the speed of light transits from one medium to another with a different medium index. In the case of the AMS TRD, these two mediums are the vacuum, and the fleece radiator [46].

Figure 3.8a shows the TR emitted when a positron passes through the TRD. AMS-02 TRD is made up of 20 layers of polyester/polypropylene fleece radiator that each of which is followed by straw tubes that are filled with Xe and CO_2 gas mixture with a ratio 80:20 respectively to detect the TR photons, which are X-rays.

A gas with high Z atom is better for the detection of these X-ray photons, and straw chambers are ideal since their attenuation of X-Rays can be minimized [47]. The TRD consists of 328 modules, each of which has 16 straw tubes, and therefore the total number of gas-filled straw tubes in TRD is 5248. To obtain 3D tracking, the upper and lower four layers of TRD are aligned in the bending plane parallel to magnetic field of AMS and the middle 12 layers are perpendicular [48]. TRD can distinguish positrons from protons with the help of ionization rate in the gaseous with dE/dx ratio [45].

3.2.3 Silicon Tracker (ST)

Figure 3.9 shows the *Silicon Tracker (ST)*. The ST consists of 9 layers. Layer 1 (L1) is located at the very top of the AMS detector. It is also called the upper tracker. Layer 9 (L9), or in other words, the lower tracker, is located above the ECAL. Since L1 and L9 are together located at the external of the detector, they are together called the *external tracker*. Layers from Layer 2 (L2) to Layer 8 (L8) are called the *inner tracker*. L2 is located above the magnet and from L3 to L8 are located inside the magnet. As the

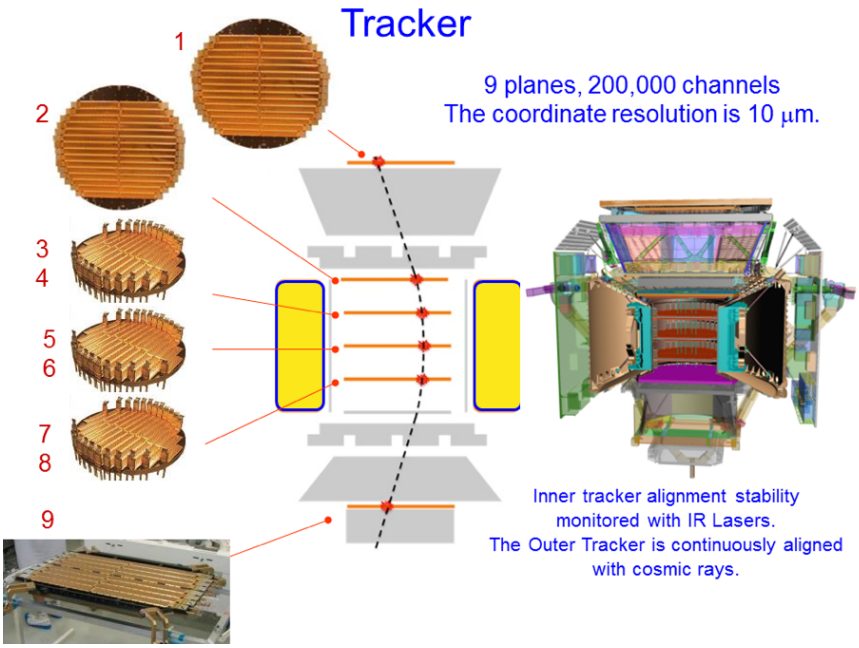

Figure 3.9: A drawing of the AMS silicon tracker with photos of each layer. Layer 1 (L1) is located at the very top of the AMS detector, the inner layers (from L2 to L8) are located inside the magnet and the layer 9 (L9) is located between the RICH and the ECAL.

name suggests, the ST tracks the trajectory of the charged particles through their hits on the layers and measures the ratio of their momenta to their charge, in other words, their *rigidity*. The ST can also measure the charge of particles and identify different nuclei species through their dE/dx depositions in the silicon.

The ST consists of 2284 double-sided microstrip silicon sensors. The silicon sensors have two sides,which are called the junction or the p-side and the ohmic or the n-side. The junction side measures the hits on the bending coordinate of the trajectory of the particle, which is namely the y-coordinate which after reconstruction of the track allows for a measurement of rigidity. On the other hand, the ohmic side measures the hits on the non-bending coordinate which is the x-coordinate.

When a charged particle interacts with the tracker, it losses energy according to the Bethe-Block formula (equation 2.4.1) and this energy is registered as hits on the sensors, which is collected in a cluster of read-out strips. If one sums the cluster signals individually up, the total cluster amplitude can be found. The total cluster ampli-

tude is proportional to the amount of energy lost by the particle. Since $dE/dx \propto Z^2$, distinguishing different types of nuclei with ST becomes possible [49].

3.2.4 Rich Imaging Cherenkov Detector (RICH)

The RICH is responsible for measuring the charge and the velocity of the particle independently. It is located between the lower ToF and the ECAL. Figure 3.10 shows the RICH detector and its components. The RICH is composed of three main parts, which are a radiator, a reflector which is in a conical shape and a detection plane. Its working principle is based on the Cherenkov radiation which was mentioned in section 2.4. If the Cherenkov speed of a relativistic charged particle in the RICH radiator medium is greater than that of light, Cherenkov radiation is emitted in a cone around the track. This radiation is detected directly by the detection plane directly or after reflection on the conical mirror. The velocity of the particle is found by reconstructing the ring of the Cherenkov cone from the hits in the detection plane and the direction that is measured by the ST [50].

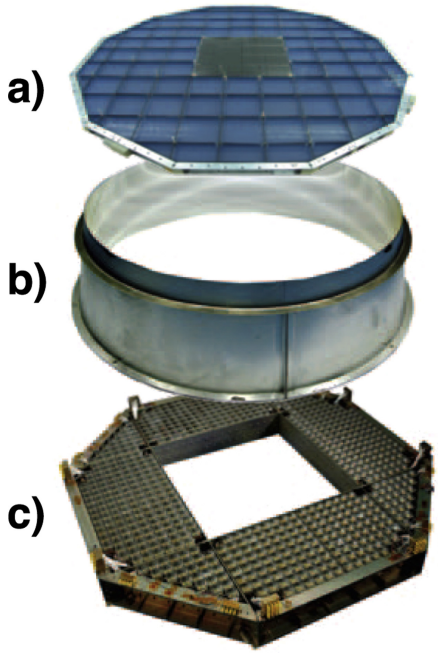

Figure 3.10: AMS RICH detector where (a) shows the radiator, (b) the reflector and (c), the detection plane. When the Cherenkov radiation is emitted in a cone around the track, it is detected directly by the detection plane or after reflection on the conical mirror. [51]

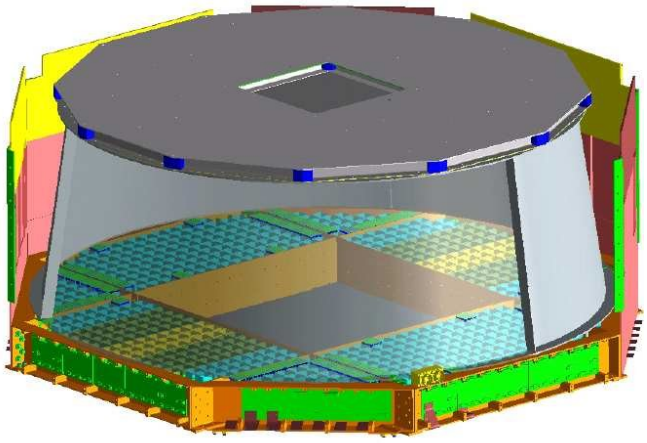

Figure 3.11: The combined view of the AMS RICH detector where the radiatior is located at the top and the reflector in the middle. At the end the detection plane is located [52]

3.2.5 Electromagnetic Calorimeter (ECAL)

The ECAL, which is located under the L9, is a 3D sampling calorimeter made of lead and scintillating fibers which can be seen in figure 3.12 and responsible for measuring the energy of high energy photons, positrons and providing proton background rejection for positrons. At the only one end of each fiber, there are photomultipliers that collect the light and turn it into a signal [53]. With 18 layers in the longitudinal direction and 72 layers in the lateral direction, the ECAL has a high granularity. The shape of the shower in the ECAL is used for classification of the particles. The ECAL has a crucial role in identification of photons [54].

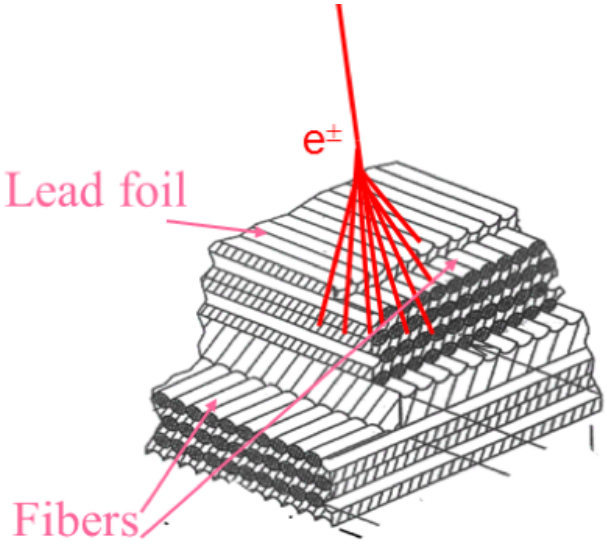

Figure 3.12: A model that demonstrates a shower in the AMS ECAL. The fine layering of the lead and scintillating fibers allow the high granularity of the ECAL. The shower created in the ECAL by the interaction of an electron or a positron can be seen.

3.2.6 Anti-Coincidence Counter (ACC)

The ACC is a veto system for the trigger to eliminate unwanted high angle events that are detected by AMS-02. Particles entering the detector sideways or particles with a trajectory that cannot be reconstructed as it does not have enough hits in the tracker

are examples of such unwanted events. The ACC adjoins the ST in order to reject particles coming from the sideways of the detector or secondaries produced inside the detector. Another task of ACC is to shorten the trigger time of the experiment in regions like the SAA since the flux in these regions is highly increased. [55].

3.3 Data Acquisition and Monte Carlo Simulation Program

After the relevant AMS subdetector electronics is triggered by a particle, the information read out from that subdetector is collected and is a called raw event. The raw events are collected in runs and each run has a matchless 32bit identifier. One run contains the events that are collected in 23 minutes which is a quarter of the total orbital duration of the ISS. This corresponds to approximately 700,000 events which increases in locations like the SAA and close to the poles. The collected *raw data* is sent to the Marshall Space Flight Center, as was mentioned in Section 3.1. At the end, the data is collected at the POCC. With specialized analysis software, the measurements contained in the raw data are related to ordinary physics quantities such as charge, velocity, energy and momentum [56].

The AMS Monte Carlo (MC) is a simulation program based on GEANT4. It is used to simulate the hadronic and the electromagnetic interactions of detected nuclei with the sub-detectors of AMS-02. The output of the MC is designed to be very similar to the data format of the flight data. These produced events are treated just like the events collected by the ISS. Comparing the ISS data and the simulated MC, it is possible to compute the ratio between these two and therefore compute efficiencies for each of the subdetectors [57].

CHAPTER 4

TIME INDEPENDENT HELIUM FLUX ANALYSIS

Helium is the second most abundant nuclei among the charged CR composition with 12%, 4% of which comes from Big Bang nucleosynthesis, and a primary nuclei and its main producer and the accelerator is thought to be supernova remnants. Maximum Detectable Rigidity(MDR) of helium is 3.2TV and it has a small interaction cross-section[58], therefore it is important to analyze the helium flux in the GV-TV range to understand its origin, propagation and acceleration [59].

For the helium flux analysis, the first step is applying general data quality cuts to the data set which are called pre-selections. After that, cuts specific to selecting helium nuclei must be applied. Then, the *exposure time* and *sub-detector efficiencies* as well as the effect of cumulative cuts for the data measured by AMS-02 must be computed. The same procedure shall be performed for the MC simulation, and the cuts be displayed separately. After that, the resulting efficiencies for the AMS-02 data and the MC simulation will be compared, and the ratio between these two will be discussed. Next comes computing effective acceptance. To compute effective acceptance of the MC, migration matrix will be obtained and will multiplied by the *geometric acceptance*. Next, the unfolding procedure will be performed using the migration matrix to obtain the helium flux. By using the migration matrix, the acceptance is unfolded and the helium flux is obtained.

4.1 Analysis Method

Helium flux Φ_i can be expressed as equation 4.1.1

$$\Phi_i = \frac{N_i}{A_i \epsilon_i T_i \Delta R_i} \tag{4.1.1}$$

where i denotes the i^{th} rigidity bin in the rigidity interval (R_i , $R_i + \Delta R_i$) where N_i denotes the number of helium events selected, A_i is the effective acceptance, ϵ_i is the detector efficiency and T_i is the time that detector collected events [60]. The analysis starts with the *raw data* which is subjected to a series of cuts to obtain good quality helium events. Cuts can be categorized into specialized cuts for the type of analysis that is performed and generic cuts to obtain good quality events. To start with, the quality of the data set that is used should be checked and for that purpose, the runs that are labelled as *bad runs* by the AMS-02 collaboration should be removed from the run list. These bad runs result from suboptimal operating conditions of the sub-detectors such as an alignment issue in the tracker. By using the list provided by the AMS-02 collaboration, the runs 1306219312, 1306219522, 1306233745 and 1307125541 $\leq$ *runs* $\leq$ 1307218054 are removed for AMS-02 operational conditions, run 1321198167 is removed for bad operating conditions for the ECAL, 1434801178 $\leq$ *runs* $\leq$ 1434841341 are removed due to the trigger system being in the wrong configuration. Another requirement is AMS-02 being operating in normal conditions and the angle that is between AMS-02 and the local zenith should be within 40° and the data acquision live-time should be greater than 0.5. Maximum alignment difference for external layers should be L1 and L9 is 3.5x10^{-5} m and 4.5x10^{-5} m respectively to keep the external tracker aligned with the inner tracker [3].

The data set under study here starts from the launch of AMS-02 (16 May 2011) and extends up to 6th of June 2020, which corresponds to 108 months and 21 days of data taking. The version of the reconstruction of data is version B1130, pass7. This data set also includes the data published by the collaboration, which extends up to 2013 [61], but is much longer in time. The MC, on the other hand, is produced in version B1200 He^4. This analysis will use the ToF, the L1 and the L9, the inner tracker sub-detectors and therefore cuts are specified for these sub-detectors.

4.2 Sub-Detector Selections

AMS-02 collaboration publishes the common selection cuts for different analyses on the web site after discussions in weekly group meetings. Since AMS continues to collect more statistics everyday in operation, these cuts may change from time to time.

4.2.1 ToF Selections

In addition to the general cuts presented in the previous sections cuts are implemented on the four layers of, ToF to increase the quality of the measurement.

The first cut is named **4/4**, to remove helium candidates which hard-scattered or disintegrated in the AMS volume. That is ensured by having only one cluster in each of the four layers of the ToF, which checks that the nuclei at the beginning of the upper ToF are the same nuclei at the end of the lower ToF. If these nuclei scattered within the detector, they would create secondaries, which would result in more than one cluster. This cut helps to eliminate the contamination from other particles.

The second cut is β **> 0.3** which eliminates upgoing particles. This cut avoids counting particles that hard-scattered with the detector as well as albedo particles from the Earth as secondaries.

The third cut concerns the number of clusters that are called "in time", **intime** $\geqslant$ **4**. In the 4/4 configuration, each selected cluster should result from the particle that is being analyzed. In other words, the time that passes from the moment of detection of the particle in the upper ToF detector, to the detection in the lower ToF, must be in an interval that is less than 10ns in order to make sure that signals are from the same particle.

The last cut concerning the ToF detector is the charge selection, $\mathbf{Q}_{ToF}$ **> 1.25**, which confirms that the selected events for helium with $Z = 2$ are not contaminated by other particles, especially by the protons.

4.2.2 External Tracker Selections

As is mentioned in section 3.2.3, the silicon tracker(ST) consists of nine layers and L1 and L9 which are located externally are called external tracker layers. If an analysis includes L1 + Inner Tracker + L9, this analysis is called *Full Span* [62]. ST is mainly responsible for measuring the rigidity of an incoming particle. To analyze rigidity better, in theory one could either increase the magnetic field or the analyzed length of the trajectory of the particle. Considering the AMS-02 layout, the maximum trajectory length that can be obtained is the full span configuration, and therefore the maximum rigidity resolution [63]. This configuration also makes it possible to reach *Maximum Detectable Rigidity*, and it is 3.2TV for Helium nuclei.

The first cut used for external tracker efficiencies is **XY Hit** which makes sure that there are hits on both bending and non-bending planes of the tracker layers. The second one is called **good Q hit**, or **good Q status**, which checks that the trajectory of the particle can be reconstructed good enough to enable calculating the charge of the particle. The third cut is $\boldsymbol{\chi^2 < 10}$, which limits how much the particle deviated from the reconstructed trajectory. The last cut is on charge selections, $\boldsymbol{1.7 < Q_{L1} < 2.5}$ for and $\boldsymbol{1.7 < Q_{L9} < 2.5}$ for L9, which are responsible for minimizing the contamination of other nuclei in the same way that was applied to the ToF detector.

4.2.3 Inner Tracker Selections

The remaining layers of ST from L2 to L8 together are called the *inner tracker*, which is mainly responsible for determining the charge of the particle and the bending of the particle which is important in calculating the particle's rigidity in the inner tracker. So the first cut, which makes sure that the inner pattern quality is good enough to reconstruct the trajectory of the particle, which is requiring at least one Y hit on all the inner planes. With the help of this cut, it is confirmed that the measurement quality of track will be good enough to reconstruct its trajectory. The next cut, **Inner Hit > 2**, is to have at least three hits on XY sides of each layer of the inner tracker. Unlike the previous cut, this cut includes the x-direction because it contributes to charge determination. The third cut is $\chi^2 < 10$ and last and fourth cut is $\boldsymbol{1.7 < Q_{inn} < 2.5}$

with the same logic mentioned in section 4.3.

4.3 Monte Carlo Simulations for AMS-02

Monte Carlo is an essential simulation program to see the discrepancies between data and theoretical values [57]. Also, using the MC makes it possible to calculate the ratio between data and MC values and use the ratio of these values in the acceptance calculation, which is an essential parameter while computing flux. The generated MC helium spectrum here is flat. Hence, before using the MC to compute sub-detector efficiencies or acceptance, one should give the "correct shape" to the MC spectrum. This procedure is called weighting.

Weights can be thought of as the density of events in a particular bin. For each bin, the associated weight should be calculated and applied to compute the correct shape of the MC spectrum. Therefore, the first step that needs to be done is an input flux to initiate the weight calculation. The input flux should be normalized to calculate weights. Flux for each bin is divided by the total flux, and hence the normalized flux is obtained. The same procedure is done for MC events, and weight for each i^{th} bin is calculated by 4.3.1,

$$w_i = \frac{\phi_{i,norm}}{MC_{i,norm}} \tag{4.3.1}$$

and applied to the MC spectrum. The procedure left is the same as data selection and histogram filling, depending on the cuts.

4.4 Unfolding Steps

Before computing acceptance, it is useful to understand *the unfolding method*. In high energy physics, the migration effect is a common problem caused by a particular detector's limited resolution and acceptance. This effect usually occurs at low or high energies. There are two main methods to handle with this effect which are iterative unfolding and the other one is using migration matrix [64]. In order to unfold

the flux iteratively, weights are calculated as explained in section 4.3 and then they applied to a flat MC spectrum. Later, the new ratio of the ISS data and the MC simulation is calculated for each sub-detector. These new ratios are applied to the MC acceptance to calculate the new effective acceptance and the new unfolded helium flux is obtained. The procedure is repeated as long as it is needed. The second way is the migration matrix, which migrates the generated events into reconstructed ones. The disadvantage of the first method is determining a correct fitting curve. When we consider the challenges of calculating ratios in the bins less than 2.7 GV for external trackers and the ECAL rigidity construction for inner tracker, it is best to use the migration matrix method to obtain the acceptance. If the acceptance is expressed in terms of reconstructed rigidity, the acceptance is called folded, and if it is expressed as generated rigidity, it is called unfolded. In this analysis, folded and unfolded acceptance and the flux is studied with the help of a migration matrix.

4.5 Exposure Time

Exposure time or collection time is the interval that the detector operates in normal conditions and can collect signals coming from the detectors without confusion. The collection time for AMS is in units seconds since data collection is cataloged by seconds [65]. The selections that are independent of the type of analyzed nuclei, which are described in section 4.1, apply here. Also, the following need to be satisfied [66] [3]:

- **The measured rigidity value should be 1.2 times more than the maximum geomagnetic cutoff value:** This ensures only the primary particles to be selected, geomagnetic cutoff value can be calculated by using IGRF geomagnetic model.
- **AMS-02 should point in $\pm$ 40° in the local zenith:** With the choice of the angle with the local zenith, the orientation of AMS-02 is guaranteed to be in a safe data taking position. Since the altitude of AMS-02 varies with time, this alignment is important.
- **ISS being outside of the SAA:** This prevents the detector from taking false

and confusing signals. SAA is the location of the Earth's geomagnetic envelope where the Van Allen Belts come closest to the Earth's surface. Also, since the magnetic field weakens in this region, low energetic particles or, in other words, particles with low rigidity can easily reach AMS-02. Hence data acquisition saturates.

- **Live-time being > 50% :** This enables the trigger to work properly. Live-time is a measure of the fraction of time in seconds that the detector is ready to collect a new signal. Live-time varies due to the inhomogeneity of the magnetic field of the Earth, which affects the detected CR flux in that region. Low magnetic field intensity will let more CR particles enter the lower altitudes, and therefore the live-time will decrease. For example, in the SAA, the live-time almost gets closer to 0.

- **Bad runs as decided by the AMS-02 collaboration should be excluded from the data set:** The reasons for a bad run can vary, but they are mainly due to bad operational conditions for sub-detectors or the periods where tracker thermal cooling system (TTCS) was off or misconstruction of the trajectory of the particle. [67]

With these cuts applied, the exposure time in seconds for the data set "pass7" for Helium nuclei is given in Figure 4.1 against the run number and rigidity. The first blank portion of the 3D graph is around runs starting with run number 1410. The reason for this is that between the runs 1411995797-1417184590, the Thermal Tracker Cooling System (TTCS) was off and therefore runs in this condition cannot be included to exposure time by definition. For the blank portion after runs that start with 1570, are the periods with wrong tracker alignment or the TTCS is off or a ToF anomaly or a RICH test has occurred and therefore they are also excluded from the exposure time.

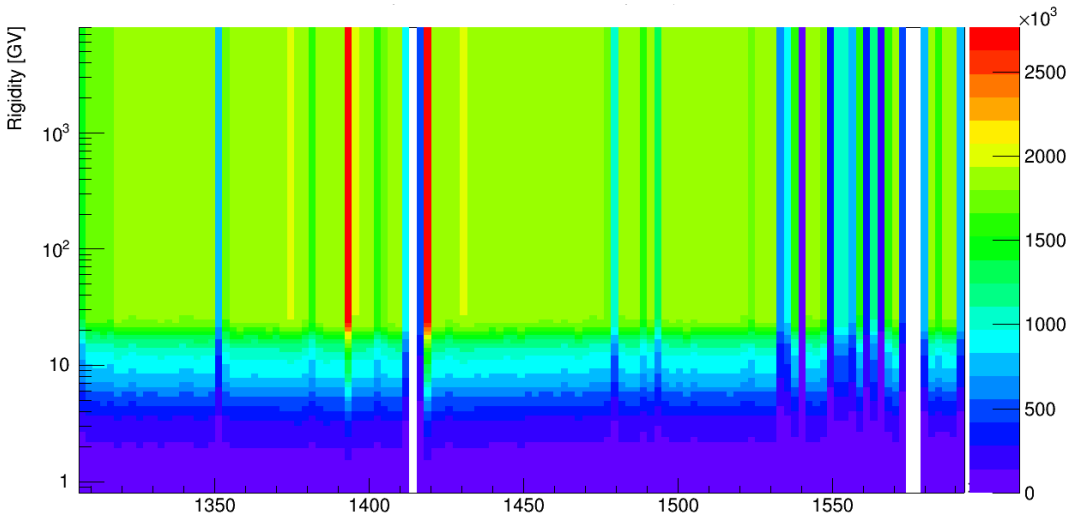

Figure 4.1: 3D exposure time plot for the latest data set "pass7" for Helium nuclei. The horizontal axis is the run numbers, the colors scale shows the exposure time in seconds and the vertical axis shows the rigidity in GV. For rigidities below 30 GV, the exposure time decreases with rigidity because of the geomagnetic cutoff and low energy particles cannot reach AMS.

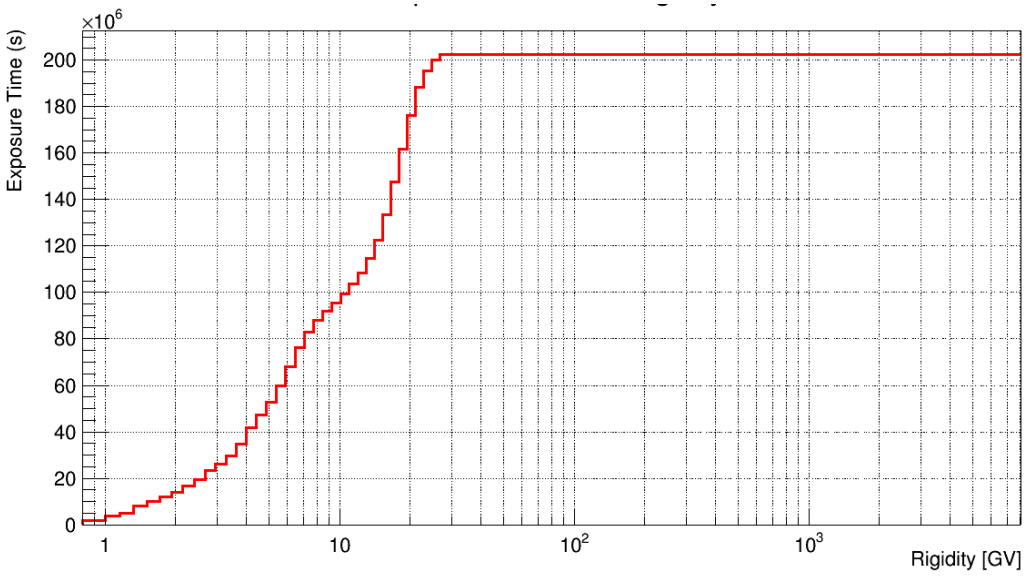

Figure 4.2: 2D exposure time for the latest data set "pass7" for Helium nuclei where the horizontal axis denotes the rigidity in GV and the vertical axis denotes the exposure time in seconds. The collection time for Helium nuclei extends up to 2 x 10^8 seconds at high rigidities beyond 30GV. Up to that point, the exposure time increases with increasing rigidity because of the geomagnetic field effect.

Figure 4.2 shows the total exposure time for Helium nuclei in 2D. The collection time for Helium nuclei extends up to 2 x 10^8 seconds at high rigidities beyond 30GV. Up to that point, the exposure time increases with increasing rigidity because of the geomagnetic field effect.

With the calculation of exposure time, one of the most important parameters in the flux calculation is completed. The next step is to compute sub-detector efficiencies for their successive and cumulative cuts.

4.6 Sub-Detector Efficiencies for Data and MC

Data based efficiency is the number of particles that passed through all the cuts except the one under investigation divided by the number of particles that passed through all the cuts in every detector.

The MC sub-detector efficiency is the number of particles that are selected by specific cuts in that detector to the number of particles that passed through its volume.

Lets remind the reader that in the flux calculation, we divide the data based efficiency with the MC efficiency to ensure a realistic understanding of the detector.

4.6.1 ToF Efficiency

In order to obtain the efficiency of the ToF detector, the specific nuclei should be unbiased and therefore the only cuts that will be applied here will be pre-selections which are previously defined in section 4.2.1. It should be noted that the cumulative effect of successive cuts will be reported here in the order as given in section 4.2.1.

Figure 4.3 shows the effect of each cut cumulatively in order, on the ToF efficiency on the ISS data. From the figure, it can be concluded that the ToF efficiency varies between 0.97 and almost 1 in the whole rigidity interval and therefore, the cuts do not have a strong effect on the efficiency of the ToF. The least restrictive cut is the four clusters requirement (4/4 in black) and the most restrictive cut is the "intime" requirement with increasing rigidity. The higher the rigidity, the more energetic is the particle and therefore, the probability of production of secondary particles increases with increasing rigidity which results in a signal which will not be in-time.

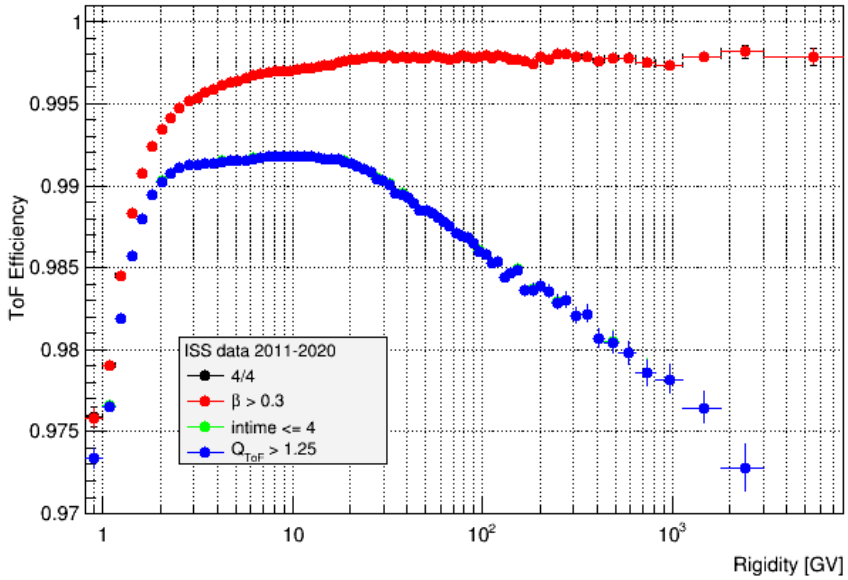

Figure 4.3: The cumulative ToF efficiency for successive cuts drawn against the reconstructed rigidity for the ISS data, with black squares showing the cut 4/4, the red showing the $\beta > 0.3$ cut , the green showing in time clusters cut and finally the blue showing the charge selection cut. The black is under the red and the green is under the blue points and cannot be seen.

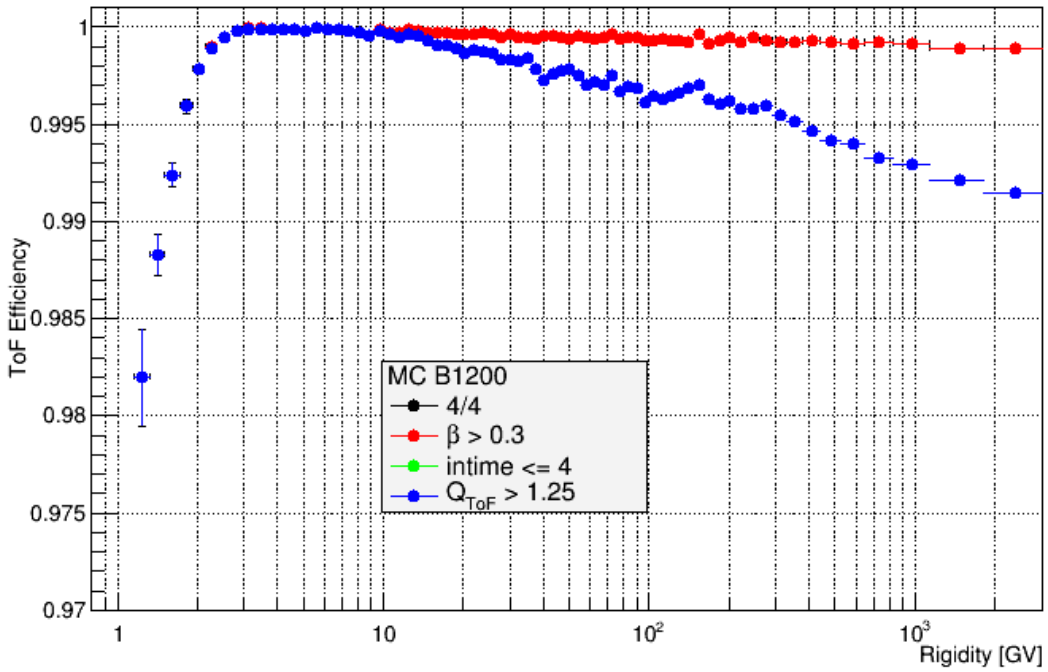

Figure 4.4: The cumulative ToF efficiency for successive cuts drawn against the reconstructed rigidity for the MC simulation, with black squares showing the cut 4/4, the red showing the $\beta > 0.3$ cut , the green showing in time clusters cut and finally the blue showing the charge selection cut. The black is under the red and the green is under the blue points and cannot be seen.

Figure 4.4 shows the ToF efficiency with the same applied cuts for the MC simulation. The efficiency for the ToF varies between 0.995 and 1, and therefore once it can be concluded that none of the cuts has a strong effect. Similar to the ISS data, the most restrictive cut is the "intime" requirement because of an increase of secondaries in the rigidity, but it can be seen that the MC underestimates the number of secondaries from the detector.

Figure 4.5 gives the comparison of the ISS and the MC ToF efficiencies with their ratio shown in the panel below. Figure 4.5 shows that both ToF efficiencies fall with the rigidity but their ratio is very flat around 99%.

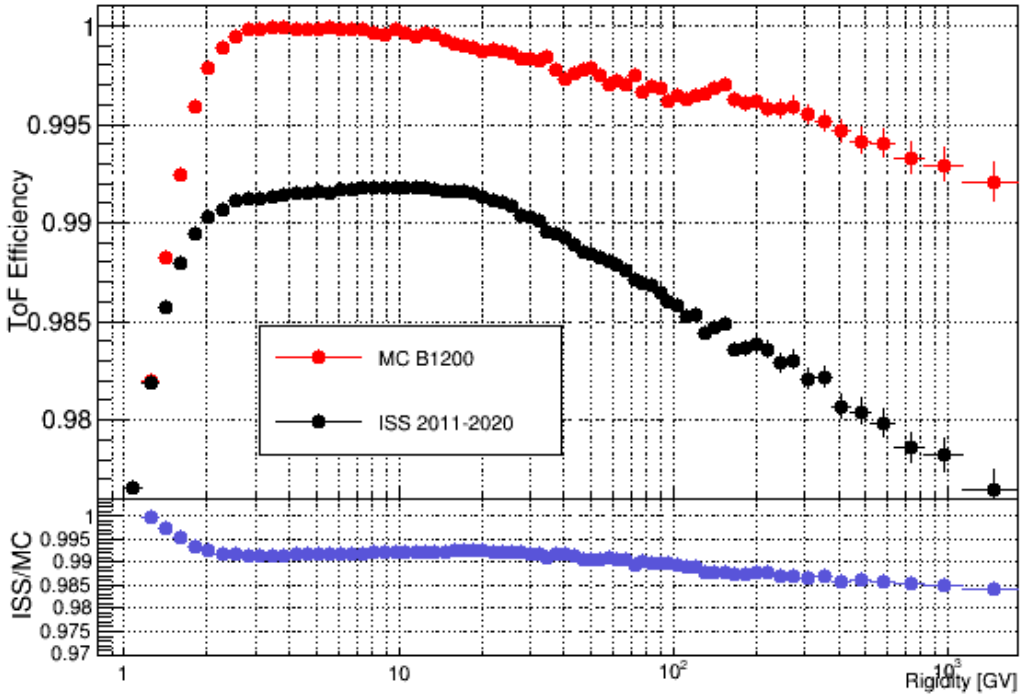

Figure 4.5: Comparison of the ISS and the MC ToF efficiencies and their ratios shown in the panel below. The ratio error is so small that it does not show in the bottom panel.

4.6.2 External Tracker Efficiencies

The next step is to compute external tracker efficiencies. In this analysis, the full span pattern is employed, and therefore L9 is also included in the efficiencies. For L1 and L9 efficiencies to be calculable, a low energy cutoff of 2.97 GV is required since lower energy helium nuclei are bent out of their acceptances by the magnetic field. Figure 4.6a and 4.6b show the cumulative effect of successive cuts for L1 efficiency on the ISS data and the MC simulation respectively.

While these two figures are similar in shape, but since the MC has a perfect tracker alignment, the χ^2 cut has little selection power as opposed to the ISS data.

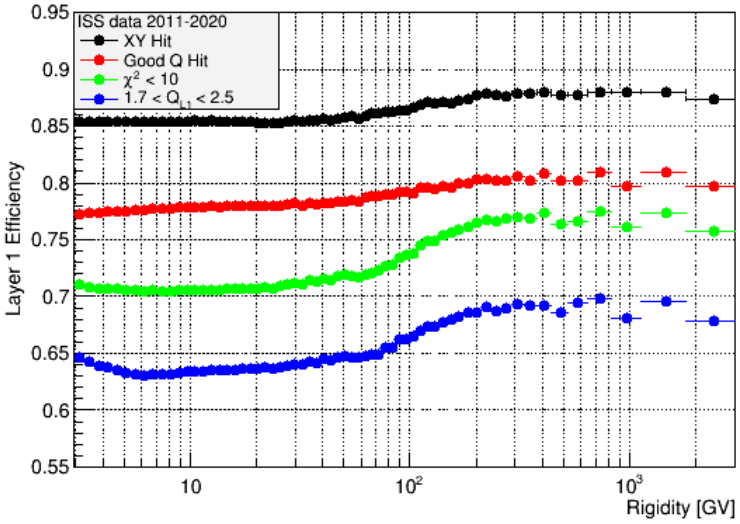

(a) The cumulative L1 efficiency for successive cuts for ISS data drawn against the reconstructed rigidity, with black dots showing the cut XY hit, the red showing charge quality cut, the green showing the χ^2 cut and the blue showing the charge selection cut.

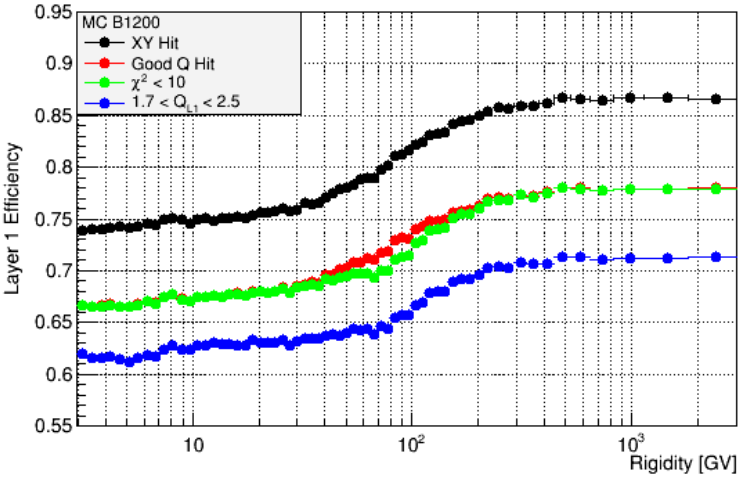

(b) The cumulative L1 efficiency for successive cuts for the MC simulation drawn against the reconstructed rigidity, with black dots showing the cut XY hit, the red showing charge quality cut, the green showing the χ^2 cut and the blue showing the charge selection cut.

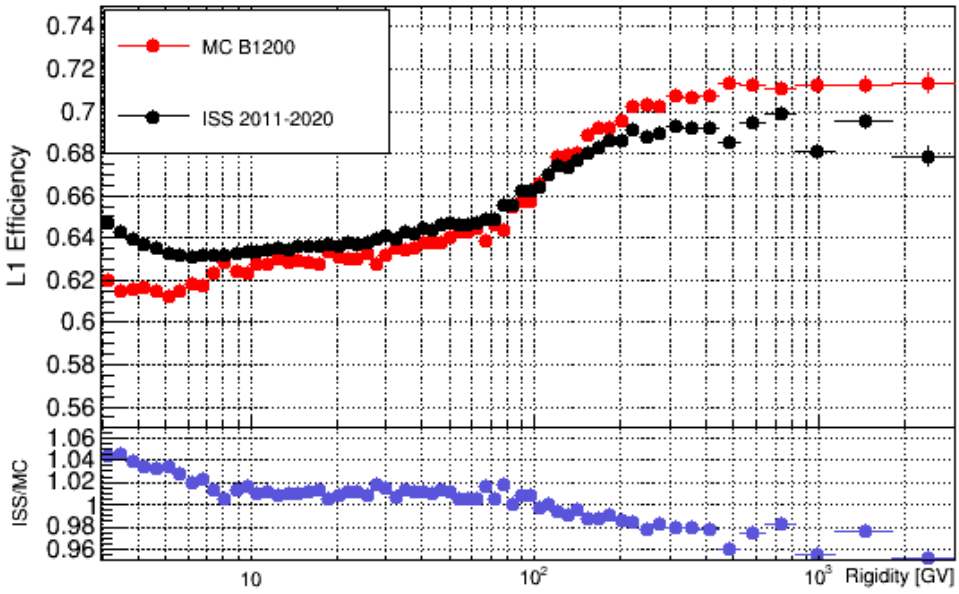

Figure 4.7: Comparison of ISS and MC efficiencies and their ratio for L1 where the black dots correspond to the ISS data for pass7 and the red dots correspond to the MC simulation where the horizontal axis represents the inner rigidity in GV and the vertical axis, the corresponding efficiency.

Figure 4.7 shows the comparison of the ISS and the MC L1 efficiencies and with their ratio shown in the panel below. It can be concluded that the ISS data and the MC simulation L1 efficiencies are compatible around 65% within $\pm 3\%$ excluding the lowest rigidity bins.

The same selections are also performed for the L9 layer. Figure 4.8a and 4.8b show the cumulative effect of successive L9 cuts for the ISS data and the MC simulation, respectively. The observations for XY Hit pattern and χ^2 cut for L1 are also valid for L9.

Figure 4.9 shows that the ISS and the MC L9 efficiencies are compatible around 58% within $\pm$ 2% excluding the highest rigidity bins. The XY Hit pattern for MC may be more restrictive due to the inefficient modelling of the detector front-ends.

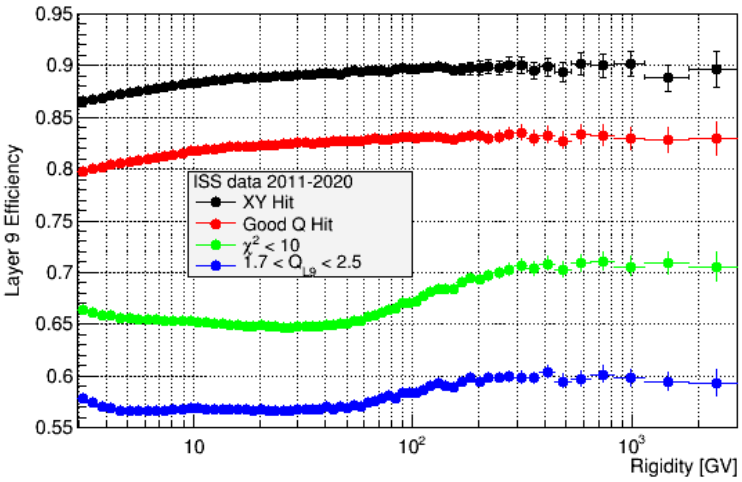

(a) The cumulative L9 efficiency for successive cuts for the ISS data drawn against the reconstructed rigidity, with black dots showing the cut XY hit, the red showing charge quality cut, the green showing the χ^2 cut and the blue showing the charge selection cut.

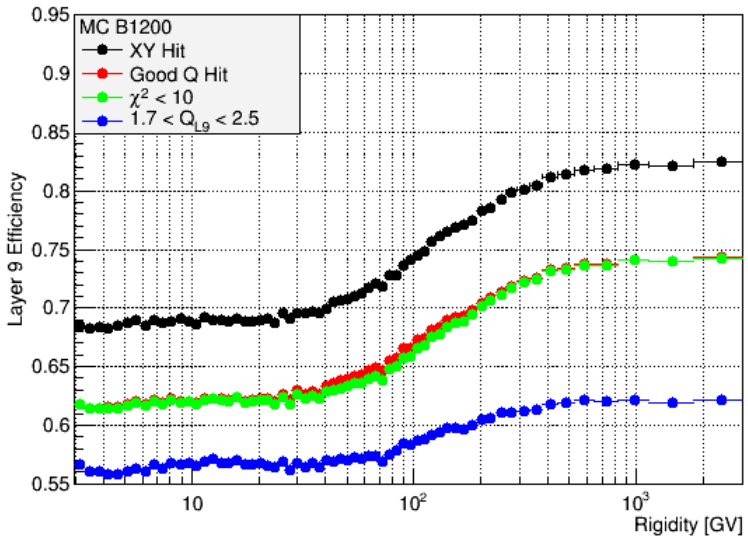

(b) The cumulative L9 efficiency for successive cuts for the MC simulation drawn against the reconstructed rigidity, with black dots showing the cut XY hit, the red showing charge quality cut, the green showing the χ^2 cut and the blue showing the charge selection cut.

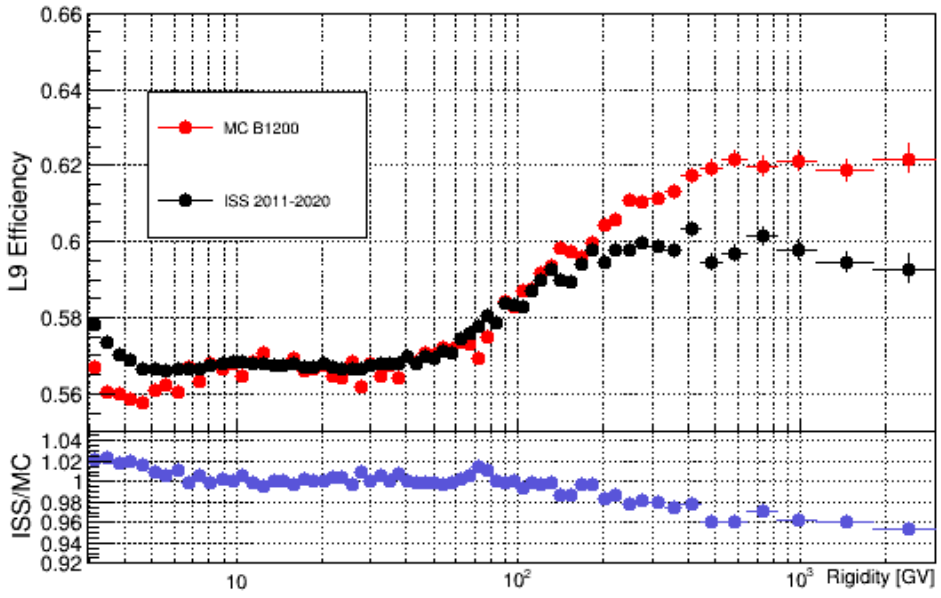

Figure 4.9: Comparison of ISS and MC efficiencies and their ratio for L9 where the black dots correspond to the ISS data for "pass7" and the red corresponds to the MC simulation where the horizontal axis the represents inner rigidity in GV and the vertical axis, the corresponding efficiency.

4.6.3 Inner Tracker Efficiency

Inner tracker efficiency is one of the hardest to compute for the ISS data because the rigidity information for the other sub-detectors is retrieved from the tracker. However, to compute the efficiency of a sub-detector, the sample nuclei should be unbiased from the sub-detector point of view, which means this detector itself cannot be used for calculations. In the case of the inner tracker, one must also use other detectors to retrieve the rigidity information.

For low rigidities, up to approximately 5.9GV, the rigidity information that comes from the β measurement of the particle in the ToF sub-detector can be used to compute the inner tracker efficiency. Recall that rigidity is p, the momentum of the particle divided by $|Z|$, the absolute charge of the analyzed nuclei. Simultaneous measurement of the rigidity and momentum of the particle allows the determination of mass

with the formula

$$pc = m\beta\gamma \tag{4.6.1}$$

$m = m_{He} = 3.727 GeV/c^2$ and $\gamma = \dfrac{1}{\sqrt{1-\beta^2}}$. Taking $c \equiv 1$, one can obtain the rigidity from the ToF detector as

$$R_\beta = \frac{m_{He}\beta}{|Z|\sqrt{1-\beta^2}} \tag{4.6.2}$$

up to a β of 0.99, which corresponds to a cutoff around 5.9GV for this method. For rigidities between 5.9GV and 19.5GV, one can use the rigidity estimated from the geomagnetic cutoff and for rigidities greater than 19.5GV, the rigidity estimation from ECAL can be used [68]. However, since the ECAL is only responsible of distinguishing electromagnetic and hadronic interactions and energy deposition in a particle shower [**?**], one cannot determine the rigidity directly from the ECAL. Rigidity must be carefully calculated from the shower and then used.

Figure 4.10a and 4.10b show the inner tracker efficiencies for the ISS data and the MC simulation respectively. From the figures, the most restrictive cut is $\chi^2 < 10$, whose data points are directly beneath the charge selection cut. Since the inner tracker tracks the trajectory of the particle and eliminates the particles with a bad reconstructed trajectory, it is understandable that the biggest inefficiency has resulted from the deviation from the trajectory.

Figure 4.11 shows that the ISS and the MC efficiencies are compatible within $\pm$ 5% excluding the lowest rigidity bins.

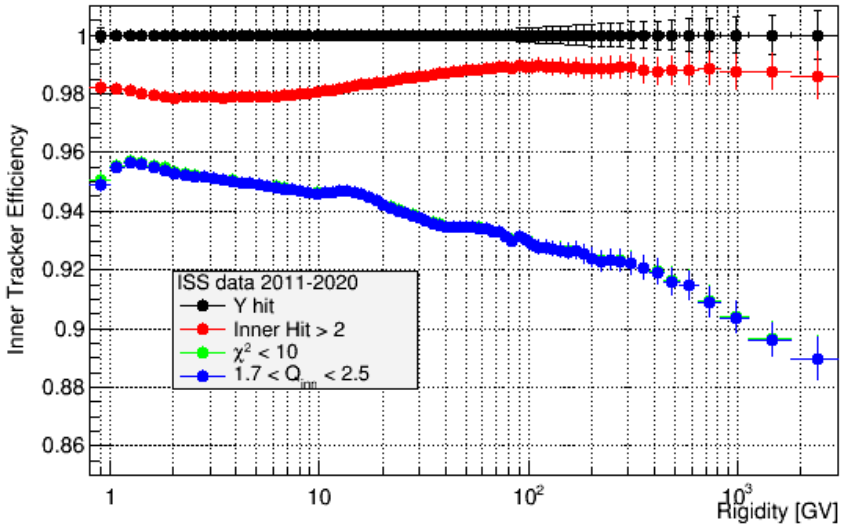

(a) Successive cumulative cuts for inner tracker for the ISS data where black dots denote the Y Hit, red denotes inner hit being more then 2, green denotes $\chi^2 < 10$, blue denotes charge selection. Green dots are under the blue that cannot be seen. Horizontal axis denote rigidity and vertical axis denotes efficiency of inner tracker.

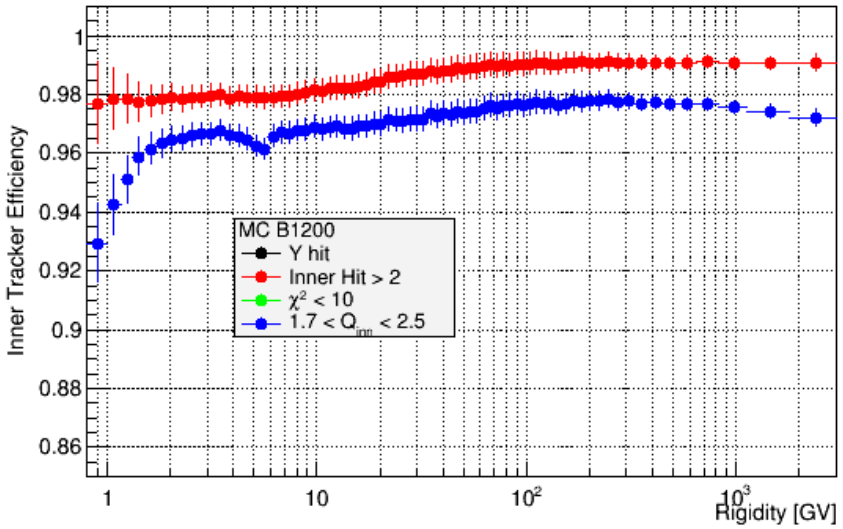

(b) Successive cumulative cuts for the inner tracker for the MC simulation where black dots denote the Y Hit, red denotes inner hit being more then 2, green denotes $\chi^2 < 10$, blue denotes charge selection. Black dots under the red and green dots are under the blue that cannot be seen. Horizontal axis denote rigidity and vertical axis denotes efficiency of inner tracker.

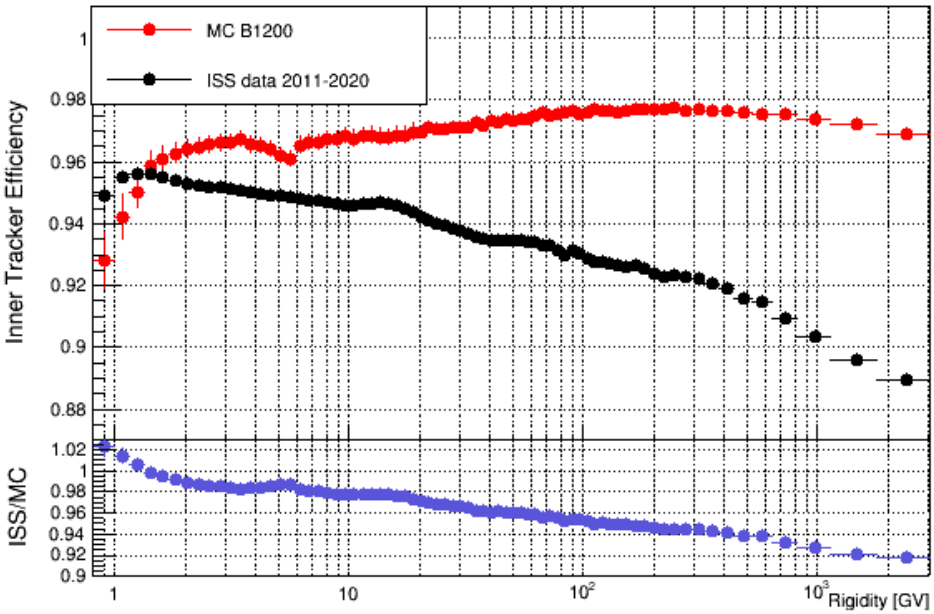

Figure 4.11: Comparison of the ISS and the MC and their ratio for the inner Tracker where the red dots denote the MC simulation and the black line denote the ISS data.

4.6.4 Trigger Efficiency

The last efficiency to be computed is the trigger efficiency. In equation 4.6.3, $\epsilon_{trigger}$ is the trigger efficiency and $N_{trigger}$ is the number of nuclei triggered, $N_{unbiased}$ is the number of nuclei that is not triggered by the detector. However, $f_{prescale}$ depends on the data used. For the ISS data, unbiased events are prescaled with 1/100 to limit the data bandwidth whereas for the MC simulation, a prescale of 1 is used which means all events are considered.

$$\epsilon_{trigger} = \frac{N_{trigger}}{N_{trigger} + f_{prescale}.N_{unbiased}} \tag{4.6.3}$$

Figure 4.12a shows the He trigger efficiency for the ISS data. The efficiency is almost 1 up to 2GV; after that point the efficiency starts to drop down to 0.94 and becomes nearly flat after 20GV. With increasing rigidity, the possibility of producing secondary particles also increases, which causes a drop in efficiency. The prescale of 100 results in a each of high statistics for higher rigidities and hence the larger errorbars.

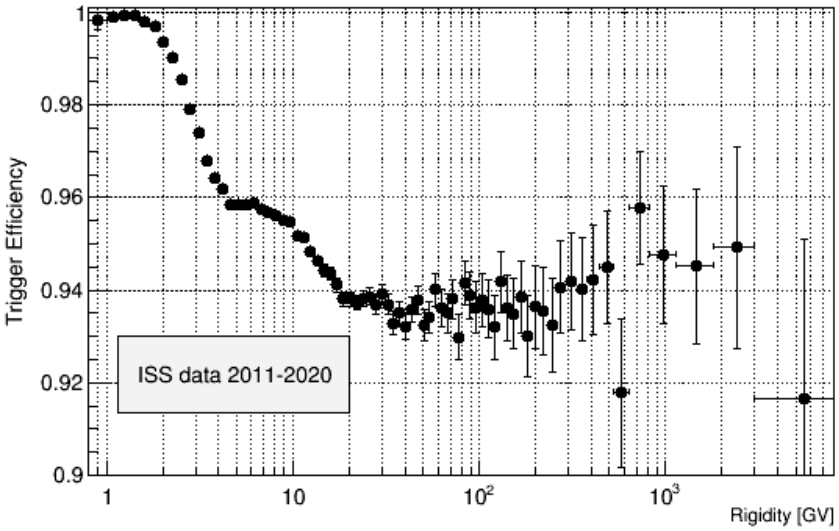

(a) He trigger efficiency for the ISS data

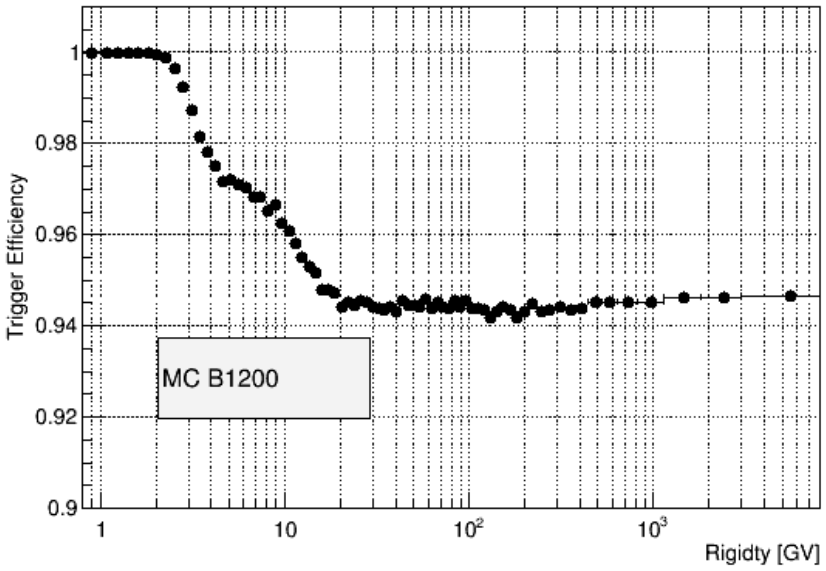

(b) He trigger efficiency for the MC simulation

Figure 4.12b shows the He trigger efficiency for the MC simulation. The MC simulation behaves in a similar fashion but there are slight differences as seen in Figure 4.13. The data and MC differ by less than $\pm$ 1%.

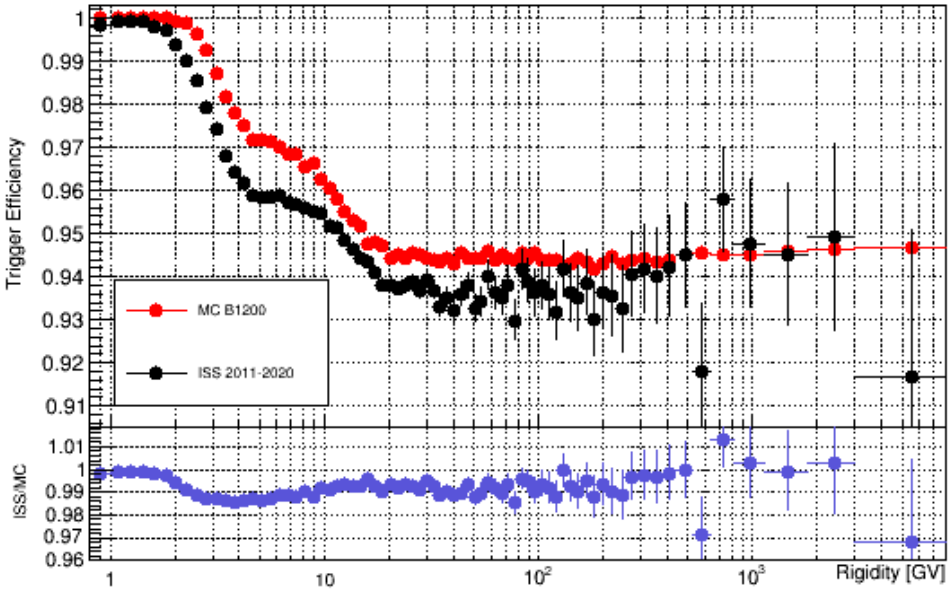

Figure 4.13: Comparison of the He trigger efficiencies from the ISS data and the MC simulation and their ratio in the lower panel

Now it is possible to proceed with computing acceptance, which is another necessary parameter to compute flux.

4.7 Acceptance

The acceptance of an experiment can be modelled in two steps. The first one, the geometrical acceptance, which only depends on the geometry of the experiment, and the second, is the effective acceptance that includes the ratio of the ISS data and the MC simulation obtained from the sub-detectors. To compute the geometrical acceptance, the MC simulation needs to be used. By using the differences between the ISS and the MC simulation, namely the ratios computed in the previous section, geometrical acceptance is corrected. The small differences between ISS and the MC simulation result from event reconstruction, selection, inefficiencies of velocity determination, tracker quality cuts and charge determination [61].

To compute the folded and the unfolded acceptances, we first determine the ratio of the selected and the generated number of particles. Then, for the generated MC spectrum, events are constructed in a cube of volume of $3.9^2\pi$ or in other words, geometrical acceptance is found. The unfolded acceptance corresponds to

$$a_{unfolded} = 3.9^2\pi \frac{N_{selected}}{N_{generated}} \tag{4.7.1}$$

and figures 4.14 and 4.15 shows the selected and generated events respectively.

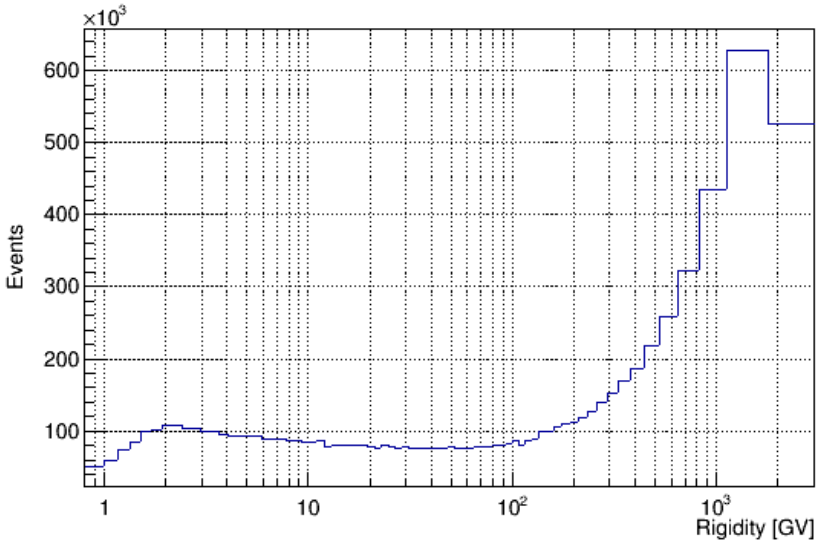

Figure 4.14: Number of selected events helium nuclei from the MC simulation

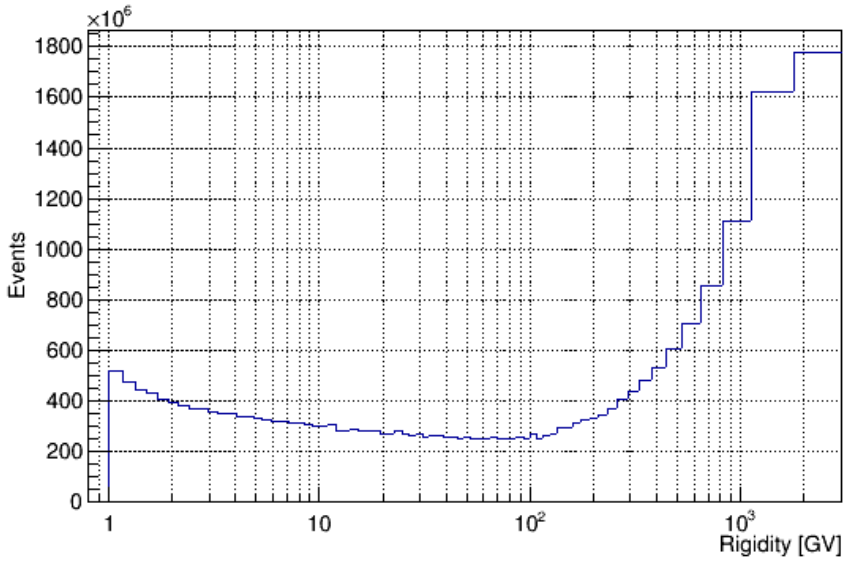

Figure 4.15: Number of generated helium nuclei in the MC simulation

In figure 4.16 unfolded acceptance with respect to the generated rigidity is shown. All statistical error bars are shown but are not visible due to high statistics.

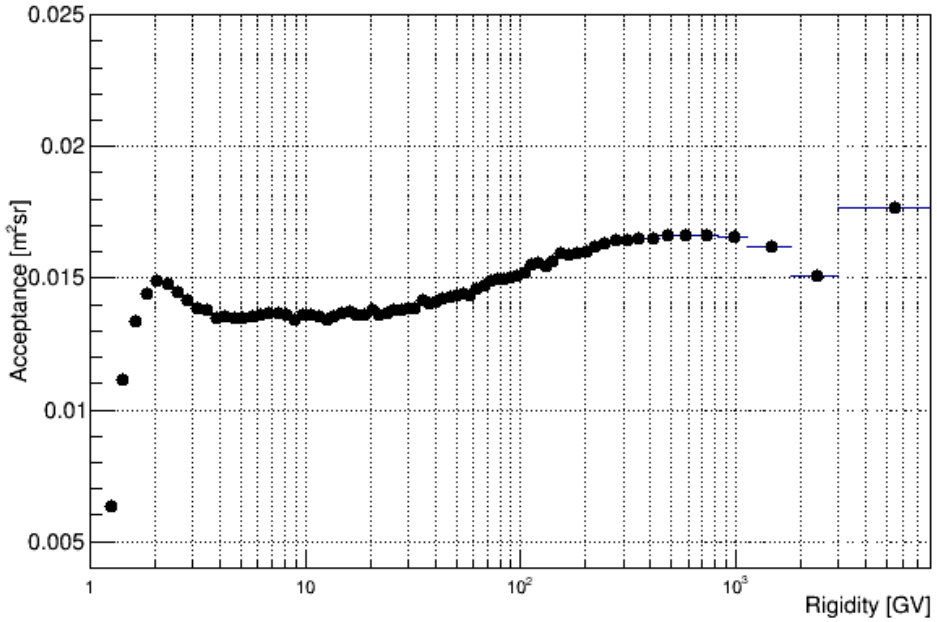

Figure 4.16: The MC (Unfolded) acceptance with respect to the generated rigidity for He nuclei

To compute the folded acceptance, the migration matrix is needed. The migration matrix represents the correlation of the reconstructed rigidity of each particle with a particular generated rigidity as obtained from the MC simulation. The migration matrix is mostly diagonal, as expected. With higher rigidity, the diagonal becomes more prominent as the bin width gets larger. Figure 4.17 shows the migration matrix for this helium analysis.

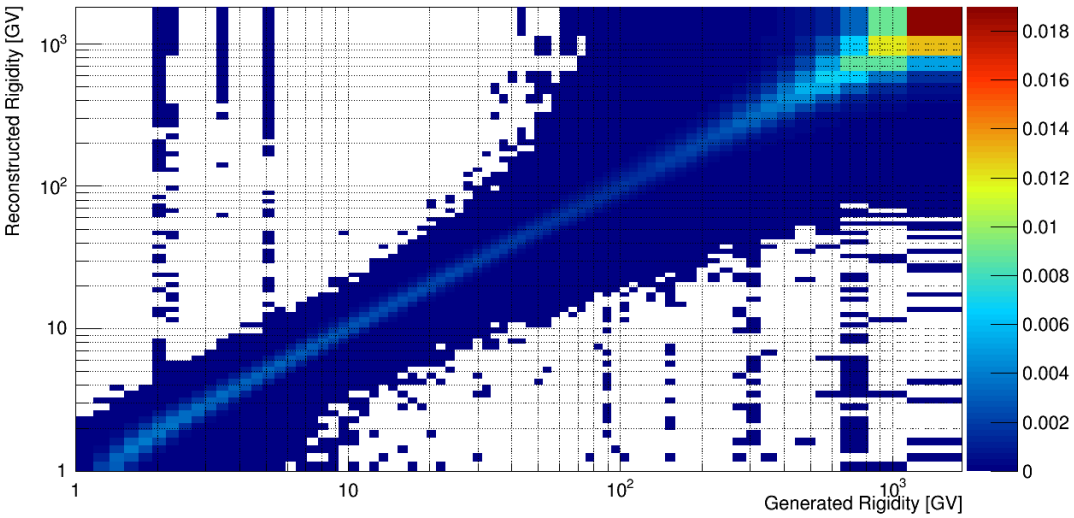

Figure 4.17: The migration Matrix for helium events in the MC

With the construction of migration matrix, the ratio of the reconstructed rigidity and the generated rigidity is found and each bin is multiplied by that ratio.

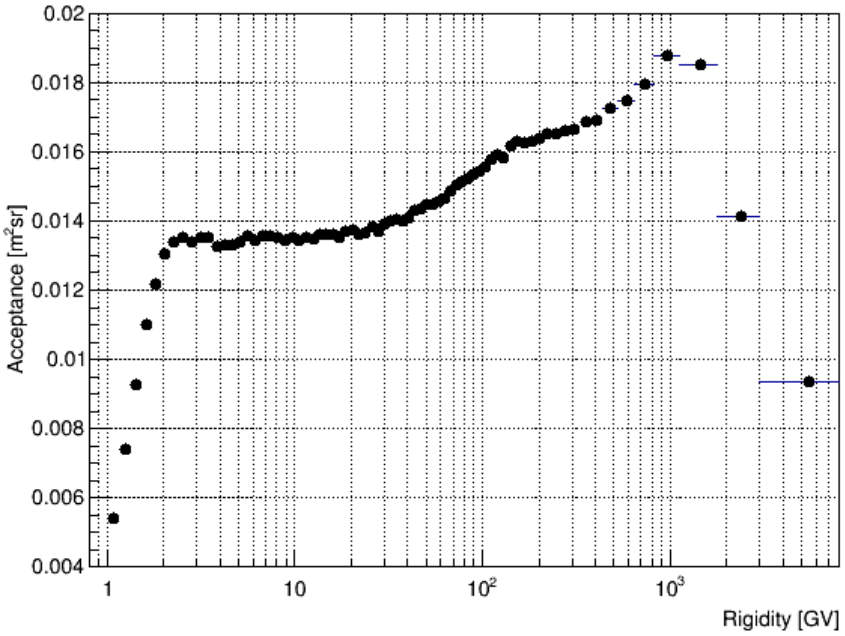

Figure 4.18: Effective acceptance with respect to reconstructed rigidity

Figure 4.18 shows the effective (folded) acceptance for helium nuclei. There is a quite difference between the effective and the MC acceptance. The fall at high energies above 1TV is due to the limited resolution of the detector. Since the number of detected nuclei is related to the acceptance of the experiment, the flux will necessarily folded acceptance.

4.8 Time-Independent Helium Flux

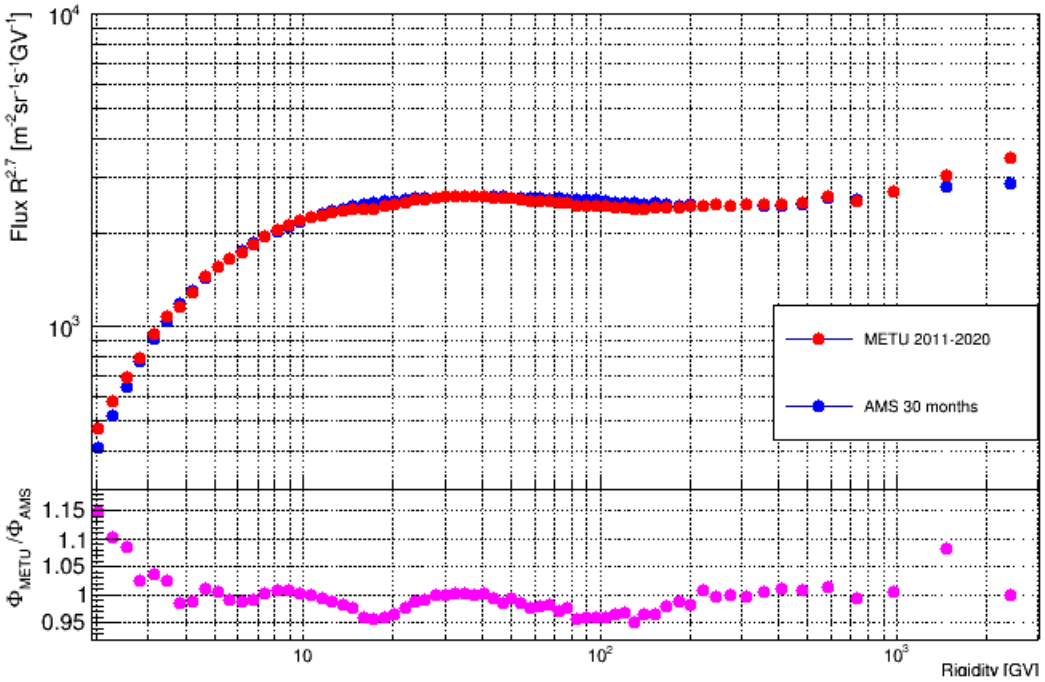

Figure 4.19: Helium flux obtained in this analysis (red) for the data set presented in a range from 2.97GV to 1200GV compared with the AMS published result for the first 30 months of operation (blue). [3]

Figure 4.19 shows the comparison of the helium flux obtained in this analysis for a dataset collected between 2011-2020 and the published AMS result for the first 30 months of operation [3]. The difference between these two results in the low rigidity bins is due to the solar modulation effect.

The range of the published flux by the AMS collaboration for the first 30 months of operation is between the 19^{th} of May 2011 and 26^{th} of November 2013 and does not include the solar maximum, which occurred in April 2014, whereas the helium data studied in this analysis starts on the same day but ends in June 2020, including both the solar maximum that occurred in April 2014 and the solar minimum that occurred in December 2019 as will be shown in detail in chapter 5. While in the 30-month dataset, the number of sunspots and therefore solar activity was increasing towards the maximum. The longer dataset, also contains the solar minimum. Therefore it is

expected that the average flux calculated by the METU group should be larger then the flux published by the AMS collaboration which also can be seen in the figure 4.19.

CHAPTER 5

TIME DEPENDENT HELIUM FLUX ANALYSIS

An observed CR flux spectrum in low rigidities can fluctuate from time to time depending on the variations of the ISM. The most dominant of these changes in these rigidities is the 11-year solar cycle. In this cycle, the CR intensity is affected by the number of sunspots as well as any change in the solar activity such as the rotation of *Corotating Interaction Regions (CIR)*, *solar flares* and *Coronal Mass Ejections (CMEs)* [69].

The Sun also exhibits other changes such as 27-day, 13.5-day and 9-day periodicities. As it is mentioned in Section 2.3.1, the 27-day of periodicity is thought to be due to the synodic rotation, which is the time interval that a fixed feature on the Sun rotates to the same position as it was viewed from the Earth. Each 27 days is called one *Bartel Rotation (BR)* [70].

In this analysis, the helium flux variability in LEO is studied for the energy range from 1.92GV to 60.3GV with the same binning choice by the AMS-02 collaboration published in [4] and the results are compared with the new data set provided by the collaboration but has not been published yet. The pass7 data set starts from the commissioning of AMS-02 (19 May 2011) and extends up to 6^{th} of June 2020 which corresponds to 108 months and 18 days of data taking and therefore 120 BRs in total. For the time dependent helium analysis, a methodology similar to chapter 4 is followed. The analysis starts with the time dependent exposure time then continues with computing the efficiencies of eacch sub-detector and the acceptance. Finally, the unfolding procedure is applied and the time dependent helium flux is obtained.

5.1 Exposure Time

The time dependent helium flux Φ_i for each BR is calculated by the formula 5.1.1

$$\Phi_i = \frac{N_i}{A_i \epsilon_i T_i \Delta R_i} \tag{5.1.1}$$

where i denotes the i^{th} rigidity bin in the rigidity interval (R_i , $R_i + \Delta R_i$) where N_i denotes the number of helium events selected, A_i is the effective acceptance, ϵ_i is the detector efficiency and T_i is the time that detector collected events for that BR. Figure 5.1 shows the exposure time for time dependent helium flux analysis.

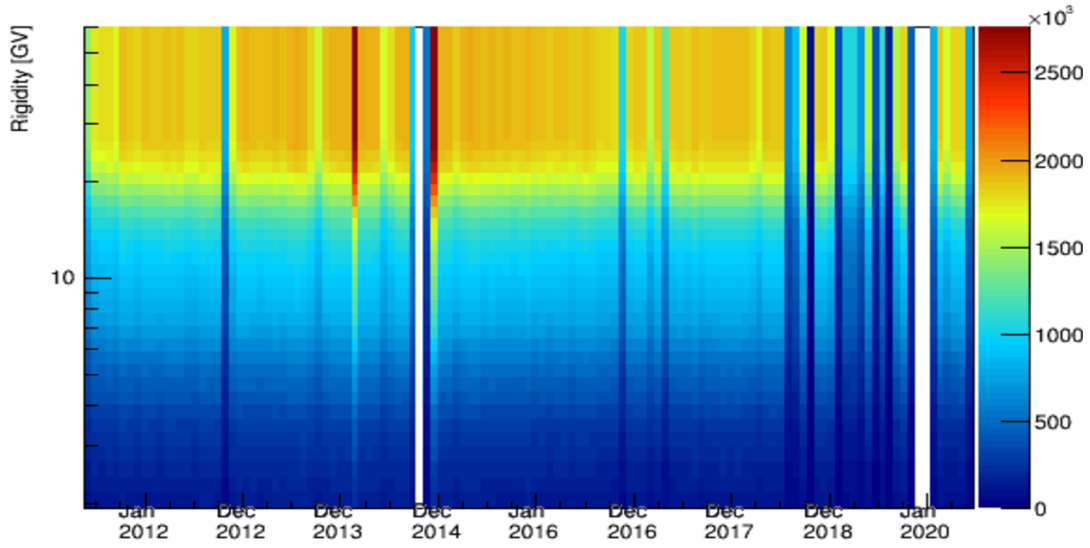

Figure 5.1: Time dependent exposure time plot for the latest data set pass7 for Helium nuclei where the x-axis denotes the dates, the left vertical axis denotes the rigidity from 1.9GV to 60.3GV and the color scale is the exposure time in seconds.

The blank portions of the plot are due to trigger issues and alignment problems that are explained in section 4.1. The exposure time stays constant after approximately 30GV due to the geomagnetic cutoff effect.

5.2 The Time Dependent Sub-Detector Efficiencies and Acceptance

In the time dependent analysis, all of the sub-detector efficiencies and the trigger efficiency must be calculated for each BR. As an illustration, the sub-detector efficiencies for 52^{nd} BR is showed in figure 5.2. The ISS data and the MC prediction are compatible within a range of 1%.

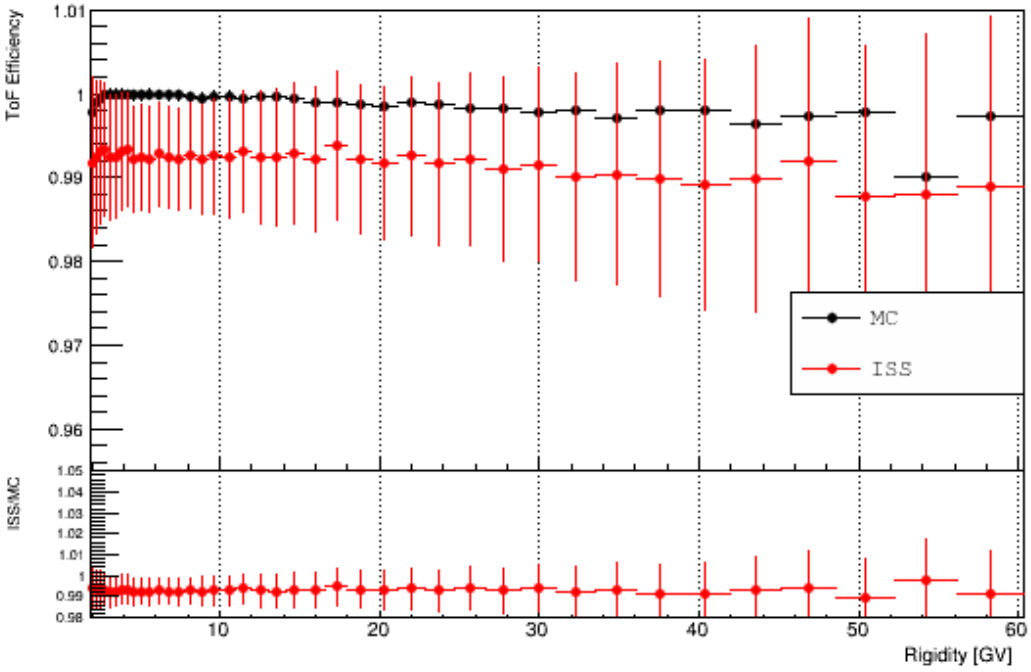

Figure 5.2: ToF efficiencies as a function of rigidity for 52^{nd} BR. The red dots denote the ISS efficiency and the black denotes the MC simulation with their ratio in the bottom panel.

Next, external tracker efficiency is computed and illustrated in 5.3 and 5.4. From the figure 5.3 and figure 5.4, it can be seen that both the L1 and the L9 efficiencies for the ISS data and the MC simulation are compatible with each other. For rigidities less than 2.97GV are not considered in the study here because the survival probability calculation requires a special configuration for the AMS-02 detector with β selected to be less than zero to detect upgoing particles.

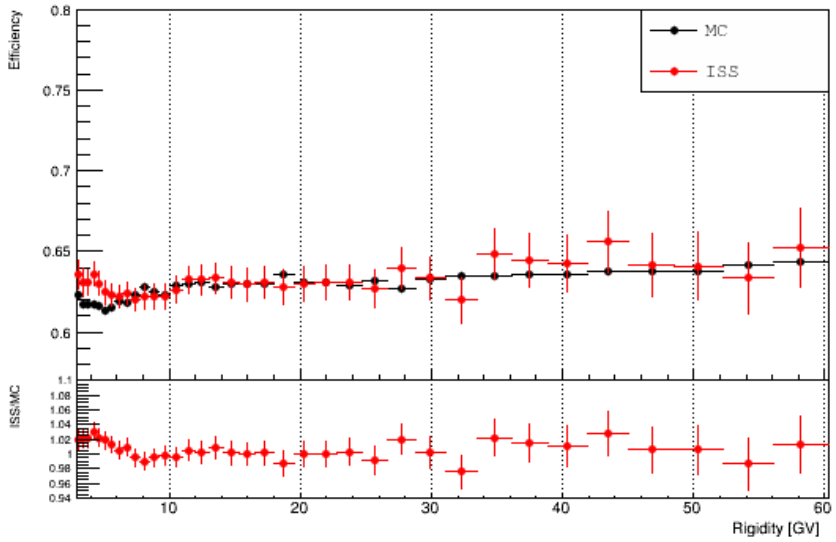

Figure 5.3: Layer 1 efficiency as a function of rigidity for 52^{nd} BR. The red dots denote the ISS efficiency and the black denotes the MC simulation with their ratio in the bottom panel.

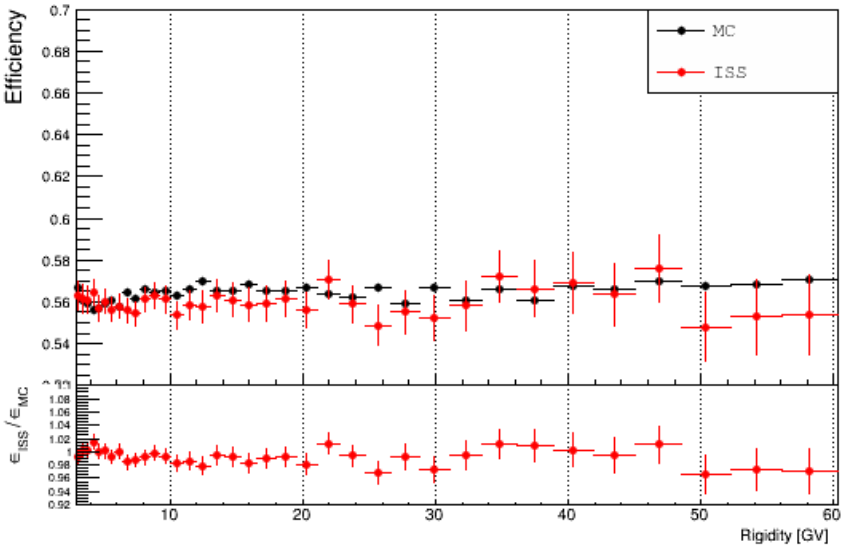

Figure 5.4: L9 efficiency as a function of rigidity for 52^{nd} BR. The red dots denote the ISS efficiency and the black denotes the MC simulation with their ratio in the bottom panel.

Figure 5.5 shows the inner tracker efficiency for time dependent analysis where the compatibility of ISS and MC values can be seen. For time dependent analysis, inner

tracker efficiency is displayed up to 19.5GV due to the difficulties of calculating the rigidity after that energy value, which requires the ECAL. The efficiency calculation for rigidities greater than 19.5GV has been performed for time independent helium analysis only.

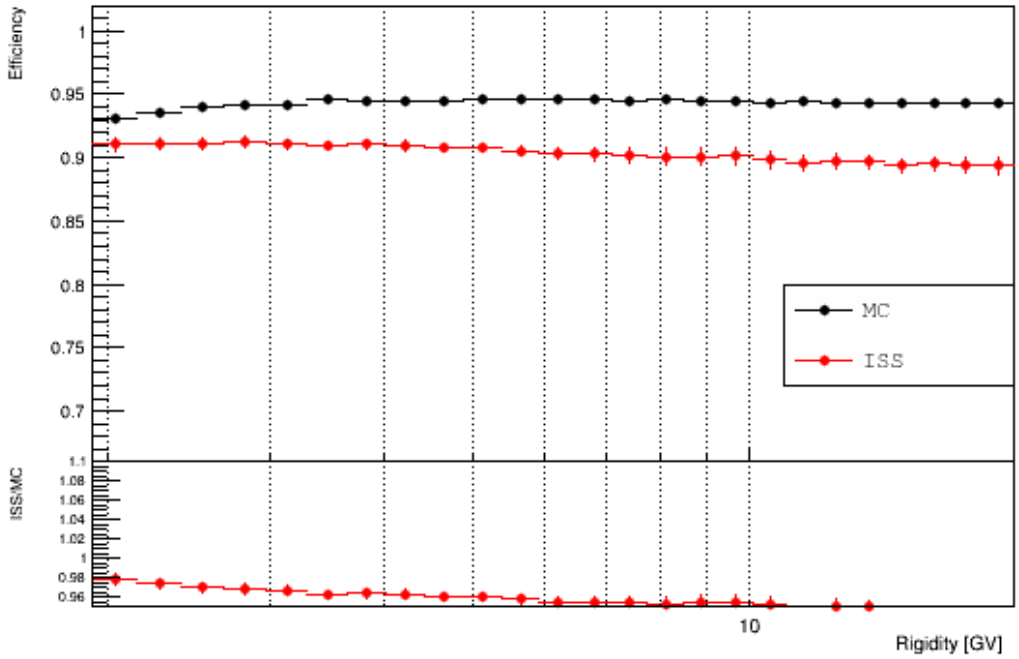

Figure 5.5: Inner Tracker efficiency as a function of rigidity for 52^{nd} BR. The red dots denote the ISS efficiency and the black denotes the MC simulation with their ratio in the bottom panel.

Next, the acceptance for the time dependence analysis is shown in figure 5.6 for the effective acceptance for 52^{nd} BR. From the figure, it can be concluded that the acceptance of the experiment in this energy range is almost constant.

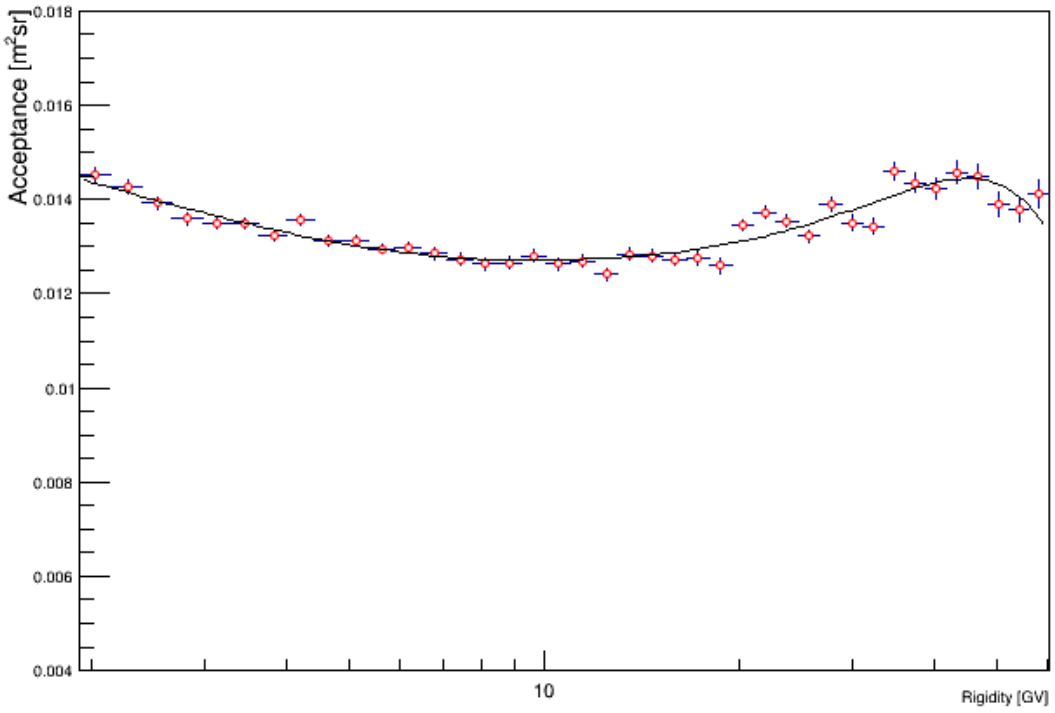

Figure 5.6: The effective acceptance as a function of rigidity for 52^{nd} BR. The acceptance in that energy range is almost constant.

5.3 Time Dependent Helium Flux

After a similar procedure is followed as described in Chapter 4, the time dependent helium flux for the latest data set pass7 is obtained and displayed within the same binning choice as the AMS-02 collaboration published in [4]. Figure 5.7 shows the time dependent helium flux for the latest data set pass7 for this analysis.

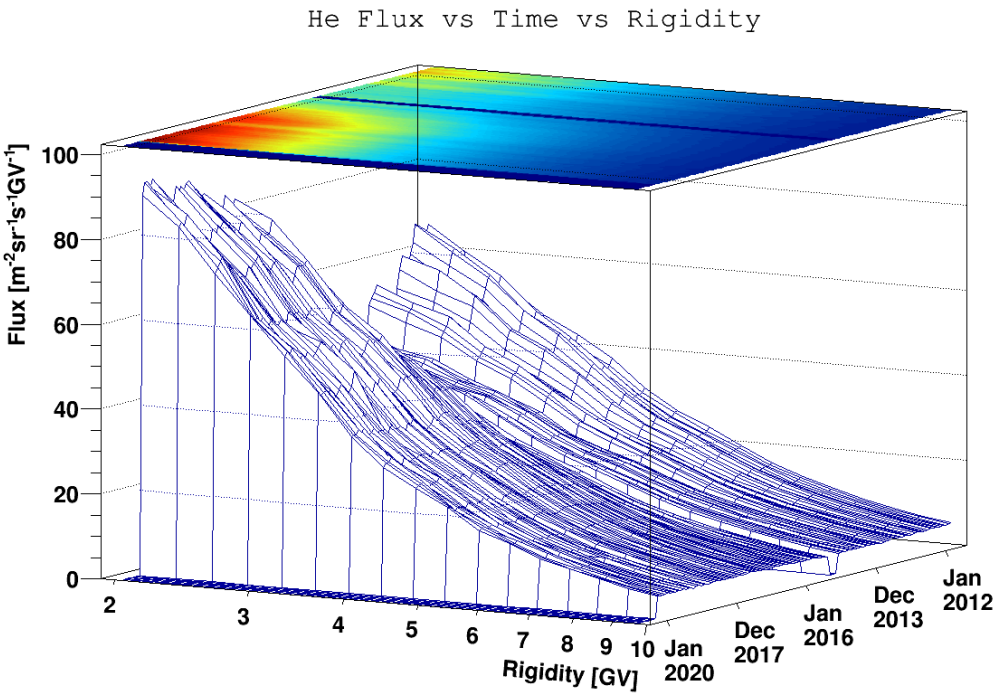

Figure 5.7: The time dependent helium flux from 1GV to 10GV from May 2011 to June 2020 for pass7 data set. In 2014, when the solar maximum occurred, the flux reaches its minimum. Towards the solar minimum that occurred in 2019, the flux climbs towards its maximum value.

From the figure 5.7, the decrease in helium flux starts from 2011 and reaches a minimum in 2014 which corresponds to the last solar maximum. After the solar maximum, the helium flux starts to increase. Figure 5.8 shows that the number of sunspots increases up to 2014 which is the definition of the solar maximum. After that year, the number of sunspots start to decrease and they reach their minimum in 2019 and correlates well with the AMS data.

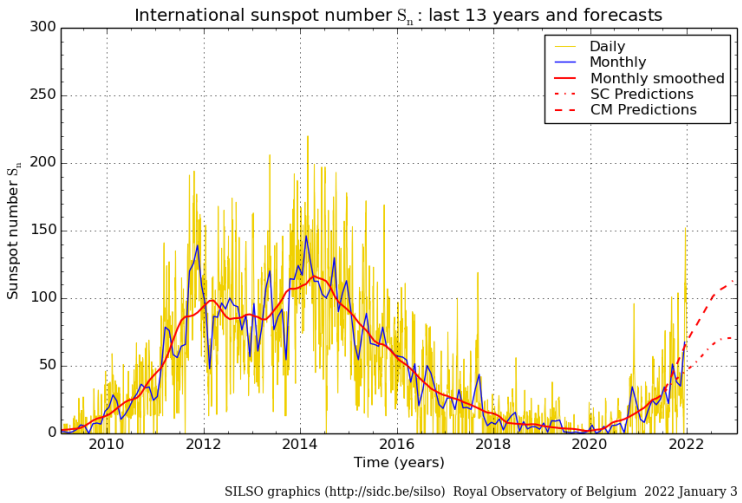

Figure 5.8: The number of sunspots in various years taken from Sunspots observed between 2009 and 2022 with several predictions. Towards the solar maximum that occurred in 2014, the number of sunspots increase. Towards the solar minimum that occurred in 2019, the number of sunspots decrease. [71]

Figures 5.9 through 5.15, show examples of the time dependent helium flux for pass7 data set from 1.92GV to 60.30GV with the same binning choice with the AMS-02. Results in each bin are compatible with the result of the AMS-02 collaboration. It can be seen that, as the rigidity increases the flux fluctuation in time decreases because the effect of the solar modulation also decreases. In low rigidity bins, the changes such as the CME, solar flares and the solar wind cause changes in the helium flux and therefore more fluctuation of the flux in time.

It can be concluded that the solar modulations in low rigidities have a large impact on the helium flux observed in LEO. Also in the solar minimum 2020, the maximum helium flux is obtained, on the contrary, minimum helium flux is obtained during the solar max in 2014.

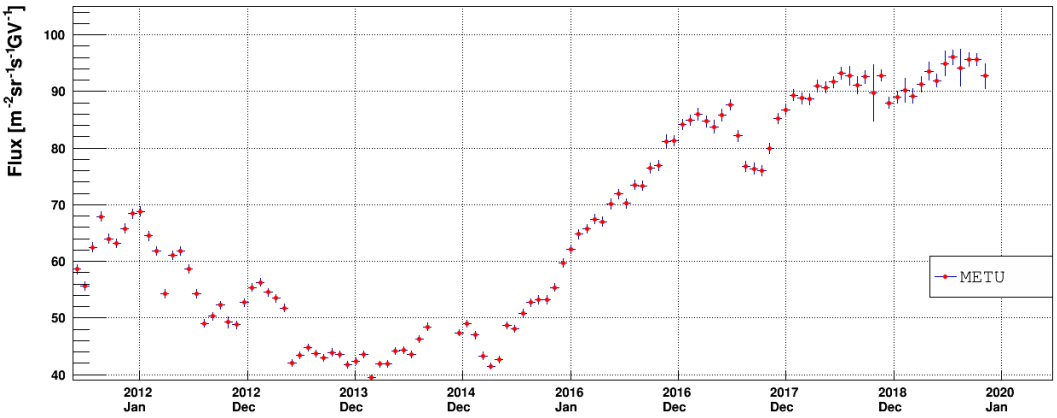

Figure 5.9: The time dependent helium flux for pass7 data set for rigidities between 1.92GV-2.15GV. From 2012 to 2014, the flux exhibits a decrease. After 2014 to 2020, the helium flux exhibits an increase as expected.

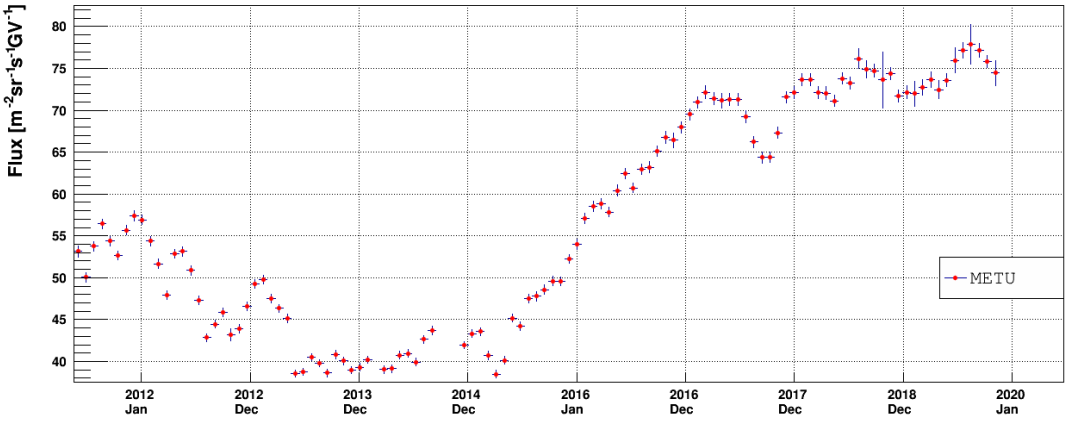

Figure 5.10: The time dependent helium flux for pass7 data set for rigidities between 2.40GV-2.67GV. From 2012 to 2014, the flux exhibits a decrease. After 2014 to 2020, the helium flux exhibits an increase as expected.

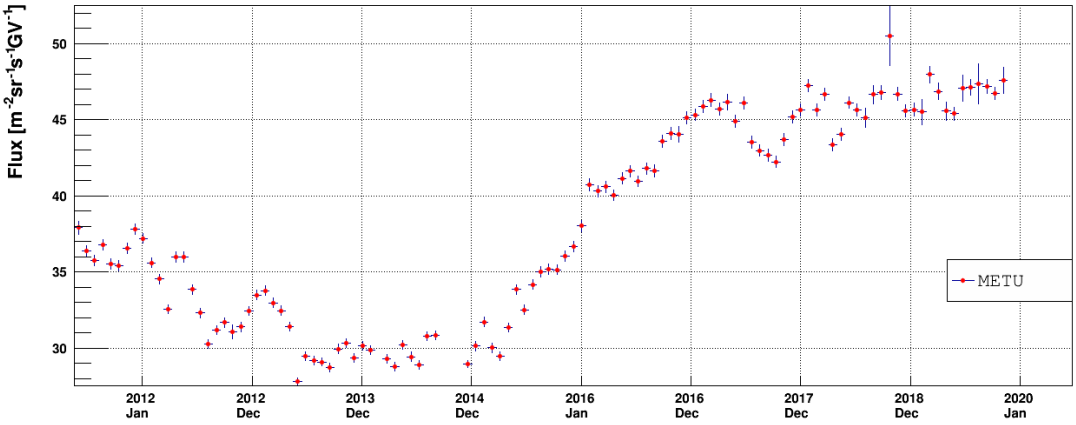

Figure 5.11: The time dependent helium flux for pass7 data set for rigidities between 3.29GV-3.64GV. From 2012 to 2014, the flux exhibits a decrease. After 2014 to 2020, the helium flux exhibits an increase as expected.

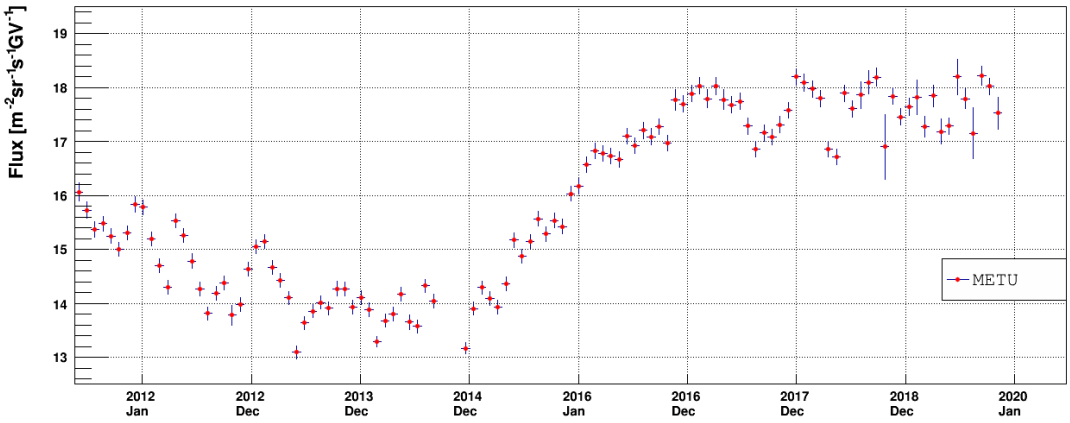

Figure 5.12: The time dependent helium flux for pass7 data set for rigidities between 5.37GV-5.90GV. From 2012 to 2014, the flux exhibits a decrease. After 2014 to 2020, the helium flux exhibits an increase as expected.

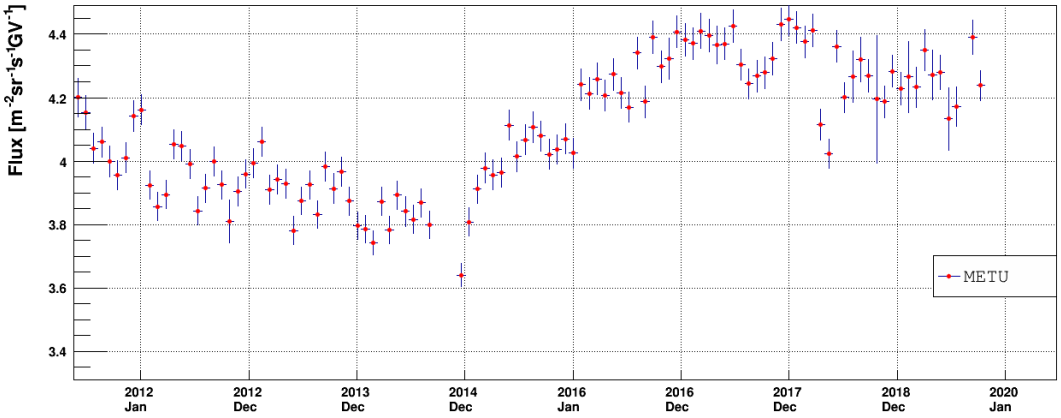

Figure 5.13: The time dependent helium flux for pass7 data set for rigidities between 10.10GV-11.0GV. From 2012 to 2014, the flux exhibits a decrease. After 2014 to 2020, the helium flux exhibits an increase as expected.

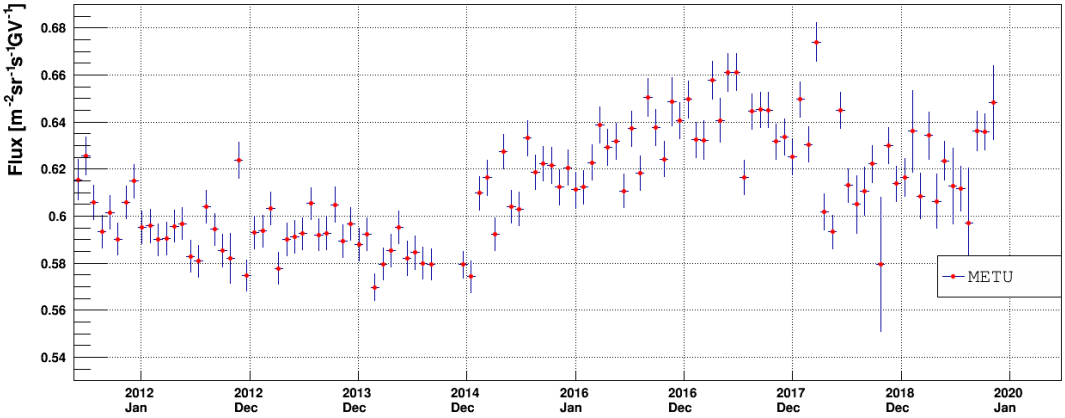

Figure 5.14: The time dependent helium flux for pass7 data set for rigidities between 21.10GV-22.80GV. From 2012 to 2014, the flux exhibits a decrease. After 2014 to 2020, the helium flux exhibits an increase as expected.

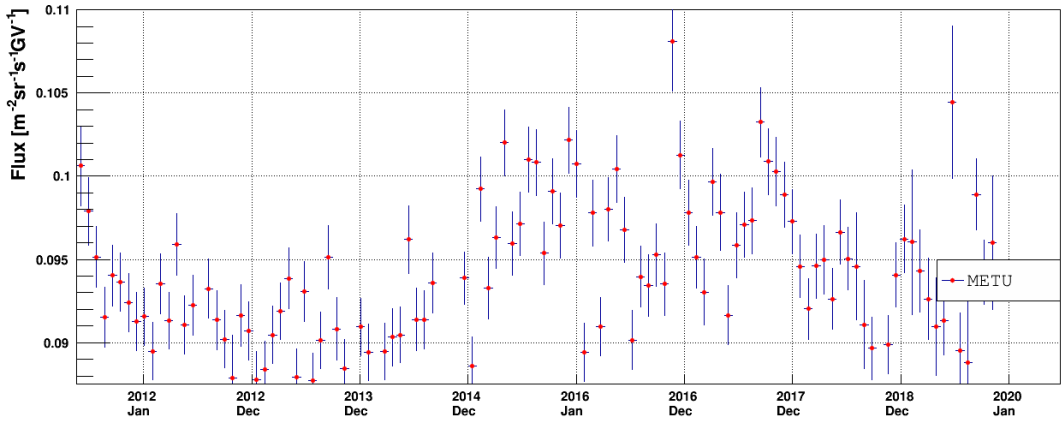

Figure 5.15: The time dependent helium flux for pass7 data set for rigidities between 41.90GV-45.10GV. From 2012 to 2014, the flux exhibits a decrease. After 2014 to 2020, the helium flux exhibits an increase as expected.

CHAPTER 6

CONCLUSION

Helium is the second most abundant charged nuclei in the CR composition with 12%. It's flux analysis with AMS-02, which is a high precision magnetic spectrometer, is important to understand the origin, propagation and acceleration of the CRs.

With the time independent helium flux analysis, the effects of applied cuts for each detector, their impact on the sub-detector efficiencies are displayed separately and cumulatively. Also the acceptance of the experiment for the helium nuclei computed and unfolding methods are also discussed. Obtained time-independent flux shows that the spectral index for the helium nuclei is rigidity dependent. The reason that the helium flux for pass7 data for this analysis is different than the published helium flux by the AMS-02 group is that datasets comprise of different time intervals in which the solar modulation causes a difference.

The time dependent flux for the latest data set pass7 is obtained and discussed for the solar maximum which occurred in April 2014 and the minimum which occurred in December 2019. The decrease of the helium flux towards the solar maximum and the increase towards the solar minimum are observed. Also the anti correlation between the solar activity and the helium flux is observed for an extended data set. The Forbush Decrease, in lower rigidity bins is observed as that the Sun sweeps away the GCRs during increased solar activity.

REFERENCES

[1] P. Carlson and A. De Angelis, "Nationalism and internationalism in science: The case of the discovery of cosmic rays," *The European Physical Journal H*, vol. 35, p. 309–329, Mar 2011.

[2] T. K. Gaisser, T. Stanev, and S. Tilav, "Cosmic Ray Energy Spectrum from Measurements of Air Showers," 2013.

[3] M. Aguilar, L. Ali Cavasonza, *et al.*, "Precision Measurement of the Helium Flux in Primary Cosmic Rays of Rigidities 1.9 GV to 3 TV with the Alpha Magnetic Spectrometer on the International Space Station," *Phys. Rev. Lett.*, 2015.

[4] M. Aguilar *et al.*, "Observation of Fine Time Structures in the Cosmic Proton and Helium Fluxes with the Alpha Magnetic Spectrometer on the International Space Station," *"Phys. Rev. Lett."*, vol. 121, p. 051101, Jul 2018.

[5] W. Crookes, "On Electrical Insulation in High Vacua," *Royal Society*, 1879.

[6] C. T. R. Wilson, "On the Ionisation of Atmospheric Air," *Royal Society*, 1901.

[7] D. Pacini, "Penetrating Radiation on the Sea," *Le Radium*, 1910.

[8] D. Pacini, "Penetrating Radiation at the Surface of and in Water," *Nuovo Cimento*, 1912.

[9] J. Lacki, "Albert Gockel, a Pioneer in Atmospheric Electricity and Cosmic Radiation," *Astroparticle Physics*, vol. 53, pp. 27–32, 2014. Centenary of cosmic ray discovery.

[10] V. Hess, "Observations in Low Level Radiation During Seven Free Balloon Flights.," *Physikalische Zeitschrift*, 1912.

[11] A. D. Angelis and M. Pimenta, *Introduction to Particle and Astroparticle Physics*. Gewerbestrasse 11, 6330 Cham, Switzerland: Springer, 2018.

[12] C. Sutton, "One Century of Cosmic Rays – A Particle Physicist's View," *EPJ Web of Conferences*, 2015.

[13] M.Schwartz, "Penumbra and Simple Shadow Cone of Cosmic Radiation," *Del Nuovo Cimento*, 1958.

[14] D. Smart and M. Shea, "A Review of Geomagnetic Cutoff Rigidities for Earth-Orbiting Spacecraft," *Advances in Space Research*, 2004.

[15] E. Fermi, "On the Origin of the Cosmic Radiation," *American Physical Society*, 1949.

[16] M. Longair, *High Energy Astrophysics*. Cambridge: United Kingdom at the University Press,, 2011.

[17] M. Malkov, P. Diamond, and R. Sagdeev, "Mechanism for spectral break in cosmic ray proton spectrum of supernova remnant w44," *Nature Communications*, vol. 2, 2011.

[18] P. Zyla *et al. Prog. Theor. Exp. Phys*, 2021.

[19] M. G. Baring, "Diffusive Shock Acceleration: The Fermi Mechanism," 1997.

[20] E. W. Cliver, "History of Research on Solar Energetic Particle (SEP) Events: the Evolving Paradigm," *International Astronomical Union*, 2009.

[21] D. V. Reames, *Solar Energetic Particles II*. Institute for Physical Science and Technology University of Maryland College Park, MD, USA: Springer, 2020.

[22] A. Belov *et al.*, "What Determines the Magnitude of Forbush Decreases?," *Advances in Space Research*, vol. 27, no. 3, pp. 625–630, 2001.

[23] I. G. Richardson, "Solar Wind Stream Interaction Regions Throughout the Heliosphere," *Living Rev Sol Phys*, 2018.

[24] A. Achterberg, "High-Energy Cosmic Rays: Galactic or Extragalactic?," *Frascati Physics Series*, 2016.

[25] A. D. Rújula, "The Cosmic-Ray Spectra: News on Their Knees," *Physics Letters B*, 2019.

[26] M. Dova, "Ultra-High Energy Cosmic Rays," *2013 CERN - Latin-American School of High-Energy Physics,*, 2015.

[27] E. Daw, "Ultra High Energy Cosmic Rays and the GZK Cutoff," 2012.

[28] A. A. Pacini, "Cosmic Rays: Bringing Messages from the Sky to the Earth's Surface," *Brasileira de Ensino de F ´ısica,*, 2017.

[29] J. Fowler, "Ionization Loss for Energetic Particles in Matter," 2009.

[30] P. Sommers, "Extensive air showers and measurement techniques," *Comptes Rendus Physique*, vol. 5, no. 4, pp. 463–472, 2004. Ultimate energy particles in the Universe.

[31] K.-H. Kampert, "Cosmic Rays In The Energy Range Of The Knee," *Astrophysics and Space Sciences Transactions*, July 2001.

[32] G. D. Sciascio, "Detection of Cosmic Rays from Ground: an Introduction,"

[33] W.Chu and G.Qin, "The Geomagnetic Cutoff Rigidities at High Latitudes for Different Solar Wind and Geomagnetic Conditions," *Annales Geophysicae*, 2016.

[34] W. Wiltschko and R. Wiltschko, "Magnetoreception in birds: Two receptors for two different tasks," *Journal of Ornithology*, vol. 148, pp. 61–76, 12 2007.

[35] C. Finlay, C. Kloss, N. Olsen, M. Hammer, L. Tøffner-Clausen, A. Grayver, and A. Kuvshinov, "The chaos-7 geomagnetic field model and observed changes in the south atlantic anomaly," *Earth, Planets and Space*, vol. 72, 12 2020.

[36] J. Heirtzler, "The Future of the South Atlantic Anomaly and Implications for Radiation Damage in Space," *Journal of Atmospheric and Solar-Terrestrial Physics,*, 2002.

[37] https://ams02.space/.

[38] https://www.nasa.gov.

[39] Gallucci, G and The ECAL Group, "Performance of the AMS-02 Electromagnetic Calorimeter in Space," *Journal of Physics: Conference Series*, vol. 587, February 2015.

[40] S. Ting, "The Alpha Magnetic Spectrometer on the International Space Station," *Nuclear Physics B - Proceedings Supplements*, 2013.

[41] M. Aguilar, G. Alberti, *et al.*, "First result from the alpha magnetic spectrometer on the international space station: Precision measurement of the positron fraction in primary cosmic rays of 0.5-350 gev," *Phys. Rev. Lett.*, vol. 110, p. 141102, 04 2013.

[42] V.Bindi, E. Choumilov, *et al.*, "The AMS-02 Time of Flight (TOF) System: Construction and Overall Performances in Space," *33rd International Cosmic Ray Conference, Rio de Janeiro 2013 The Astroparticle Physics Conference*, 2013.

[43] V.Bindi, G.Chen, *et al.*, "Calibration and Performance of the AMS-02 Time of Flight Detector in Space," *Nuclear Instruments and Methods in Physics Research A*, 2014.

[44] Hamamatsu, "Photomultiplier tubes basics and applications handbook,"

[45] T. Kirn and T. Siedenburg, "The AMS-02 Transition Radiation Detector," *Nuclear Instruments and Methods in Physics Research Section A, Accelerators, Spectrometers, Detectors and Associated Equipment*, 2004.

[46] A. Bartoloni, "The AMS-02 Transition Radiation Detector for the International Space Station," 2004.

[47] M. Demirköz, "A transition radiation detector and gas supply system for ams," Master's thesis, Massachusetts Institute of Technology, 5 2004.

[48] T. Siedenburg, "The AMS TRD. A gasdetector designed for operation in space," *Nuclear Physics B - Proceedings Supplements*, vol. 150, pp. 30–33, 2006. Proceedings of the 9th Topical Seminar on Innovative Particle and Radiation Detectors.

[49] D. Haas, "The Silicon Tracker of AMS02," *Nuclear Instruments and Methods in Physics Research A*, 2004.

[50] R. Pereira, Aguilar-Benitez, *et al.*, "The rich detector of the ams-02 experiment: status and physics prospects," 02 2008.

[51] H. Liu, J. Casaus, *et al.*, "The RICH Detector of AMS-02: 5 Years of Operation in Space," *Nuclear Instruments and Methods in Physics Research A*, 2017.

[52] F. Giovacchini, "Performance in space of the ams-02 rich detector," *Nuclear Instruments and Methods in Physics Research Section A Accelerators Spectrometers Detectors and Associated Equipment*, vol. 766, pp. 57–60, 12 2014.

[53] A. Kounine, Z. Weng, W. Xu, and C. Zhang, "Precision measurement of 0.5 GeV–3 TeV electrons and positrons using the AMS Electromagnetic Calorimeter," *Nucl. Instrum. Meth. A*, vol. 869, pp. 110–117, 2017.

[54] P. Saouter, *Nuclei Identification with the AMS-02 Silicon Tracker*. PhD thesis, Universite De Geneva, 8 2014.

[55] W. Karpinski, T. Kirn, *et al.*, "The AMS-02 Anticoincidence Counter," *Nucl.Phys.Proc.Suppl*, 2008.

[56] V. Choutko, B. S. Shan, *et al.*, "Computing Strategy of the AMS Experiment," *J. Phys.: Conf. Ser.*, 2015.

[57] J. Luo, J. Zhang, *et al.*, "AMS-02 Monte Carlo Production in Science Operation Centre at Southeast University," *IOP Conf. Series: Journal of Physics: Conf. Series*, 2017.

[58] Q. Yan, V. Choutko, A. Oliva, and M. Paniccia, "Measurements of Nuclear Interaction Cross Sections with the Alpha Magnetic Spectrometer on the International Space Station," *Nuclear Physics A*, vol. 996, p. 121712, 2020.

[59] M. Aguilar, L. Ali Cavasonza, *et al.*, "Observation of the Identical Rigidity Dependence of He, C, and O Cosmic Rays at High Rigidities by the Alpha Magnetic Spectrometer on the International Space Station," *Phys. Rev. Lett.*, 2017.

[60] M. Aguilar, L. Ali Cavasonza, *et al.*, "Precision Measurement of the Proton Flux in Primary Cosmic Rays from Rigidity 1 GV to 1.8 TV with the Alpha Magnetic Spectrometer on the International Space Station," *Phys. Rev. Lett.*, 2015.

[61] M. Aguilar *et al.*, "Precision Measurement of the Boron to Carbon Flux Ratio in Cosmic Rays from 1.9 GV to 2.6 TV with the Alpha Magnetic Spectrometer on the International Space Station," *Phys. Rev. Lett.*, 2016.

[62] M. Aguilar *et al.*, "The Alpha Magnetic Spectrometer (AMS) on the International Space Station: Part II — Results from the first seven years," *Phys. Rept.*, vol. 894, pp. 1–116, 2021.

[63] Velasco Frutos, Miguel Ángel, "Measurement of the large scale anisotropy in cosmic ray electrons, positrons and protons with the AMS-02 detector on the ISS," 2019.

[64] S. Schmitt, "Data Unfolding Methods in High Energy Physics," *EPJ Web of Conferences*, vol. 137, p. 11008, 2017.

[65] V. Choutko, A. Egorov, A. Eline, and B. Shan, "AMS Data Production Facilities at Science Operations Center at CERN," vol. 898, p. 082019, oct 2017.

[66] M. Aguilar *et al.*, "Properties of Cosmic Helium Isotopes Measured by the Alpha Magnetic Spectrometer," *Phys. Rev. Lett.*, vol. 123, p. 181102, 2019.

[67] C. Corti, *Solar Modulation of Proton and Helium in Cosmic Rays With the Alpha Magnetic Spectrometer*. PhD thesis, The University of Hawaii, 7 2017.

[68] C. Consolandi, "Primary Cosmic Ray Proton Flux Measured by AMS-02," 2014.

[69] D. Hathaway, "The solar cycle," *Living Rev. Sol. Phys.*, vol. 39, p. 227, 09 2015.

[70] Aguilar, M. and others, "Periodicities in the Daily Proton Fluxes from 2011 to 2019 Measured by the Alpha Magnetic Spectrometer on the International Space Station from 1 to 100 GV," *Phys. Rev. Lett.*, vol. 127, p. 271102, Dec 2021.

[71] https://wwwbis.sidc.be/silso/.